Materials Today Bio 32 (2025) 101793

Contents lists available at ScienceDirect

Materials Today Bio

journal homepage: www.journals.elsevier.com/materials-today-bio

Self-assembly of paclitaxel derivative and fructose as a potent inducer of immunogenic cell death to enhance cancer immunotherapy

Manzhen Li [a], Likang Lu [a], Yaoyao Guo [a], Jingxin Fu [a], Ziqi Zhang [a,b], Pengxin Li [a,c], Yifei Guo [a], Meihua Han [a], Xiangtao Wang [a,*]

[a] Institute of Medicinal Plant Development, Chinese Academy of Medical Sciences & Peking Union Medical College, No. 151, Malianwa North Road, Haidian District, Beijing, 100193, China
[b] School of Pharmacy, Heilongjiang University of Chinese Medicine, Harbin, 150006, China
[c] School of Pharmacy, Henan University of Chinese Medicine, Zhengzhou, 450046, China

ARTICLE INFO

Keywords:
Paclitaxel derivative
Phenylboronic acid
Resiquimod
Self-assembly
ICD
Chemoimmunotherapy

ABSTRACT

Immunotherapy shows promise for tumor control but is limited by low response rates. Paclitaxel (PTX) induces immunogenic cell death (ICD), yet conventional delivery systems face challenges like low drug loading and insufficient intracellular accumulation, reducing ICD efficacy. Small-molecule self-assembled PTX nanoparticles offer a promising solution due to high drug loading and dose delivery. In this study, PTX was conjugated with phenylboronic acid (PBA) to form the derivative PTX-PBA, which spontaneously self-assembled with fructose into nanoparticles (PTX-PBA-Fru NPs). These nanoparticles exhibited a uniform size of 107.8 ± 2.9 nm, a PDI of 0.064 ± 0.042, and a zeta potential of −12.2 ± 0.9 mV, with spherical morphology. In 4T1 tumor-bearing mice, PTX-PBA-Fru NPs significantly enhanced tumor inhibition ($p < 0.001$) and increased body weight ($p < 0.05$). No allergic reactions in healthy Balb/c mice and the maximum tolerated intravenous dose reached 200 mg/kg, underscoring its favorable safety profile of PTX-PBA-Fru NPs. The ICD effects induced by PTX-PBA-Fru NPs, when combined with the immunomodulator resiquimod (R848), elicited a robust anti-tumor immune response. This combination therapy effectively remodeled the immunosuppressive tumor microenvironment and achieved a 37.5 % tumor eradication rate. Moreover, it established long-term immune memory, providing protection against tumor re-challenge. This novel PTX formulation demonstrates strong anti-tumor effects, safety, and clinical potential in combination with R848-based immunotherapy.

1. Introduction

Paclitaxel (PTX) is a broad-spectrum anti-tumor agent widely utilized in clinical practice for the treatment of various cancers [1,2]. It is available in formulations such as PTX injections and nanomedicines, including liposomal PTX (Lipusu), albumin-bound nanoparticles (Abraxane), and polymeric micelles (Genexol-PM). Nanomedicine has demonstrated the ability to enhance the solubility and delivery of PTX, prolong its circulation time, and increase drug accumulation at tumor sites through the enhanced permeability and retention (EPR) effect [3–5]. These improvements contribute to enhanced chemotherapy efficacy and reduced side effects. However, numerous excipients in PTX nanomedicine result in a low drug loading capacity, typically less than 20 % (e.g., approximately 16.7 % in polymeric micelles, 10 % in albumin nanoparticles, and even lower in liposomes), leading to metabolic complications and adverse effects. For example, polyethylene glycol (PEG), an FDA-approved excipient commonly used in liposomes and PTX micelles carries potential risks such as complement activation and immunogenicity [6]. These factors constrain dosing, thereby limiting the nanoparticle-induced ICD effect.

In recent years, nanomedicines self-assembled from drugs and small molecules through non-covalent interactions (e.g., hydrogen bonds, van der Waals forces, hydrophobic interactions) have garnered significant attention [7–9]. These systems not only retain the general advantages of nanoparticles but also benefit from the unique properties of small-molecule excipients, such as well-defined structures, controllable quality, absence of biosafety risks associated with macromolecular carriers, relatively high drug loading capacity, and straightforward preparation processes [10]. For instance, a PTX-s-s-PTX conjugate was synthesized and co-assembled with 1,1-dioctadecyl-3,3,3,

---

* Corresponding author.
E-mail addresses: xtaowang@163.com, xtwang@implad.ac.cn (X. Wang).

https://doi.org/10.1016/j.mtbio.2025.101793
Received 6 January 2025; Received in revised form 27 March 2025; Accepted 22 April 2025
Available online 23 April 2025
2590-0064/© 2025 The Authors. Published by Elsevier Ltd. This is an open access article under the CC BY-NC license (http://creativecommons.org/licenses/by-nc/4.0/).

3-tetramethylindotricarbocyanine iodide (DiR) to form a novel nanomedicine with high drug loading (~78 %, w/w) and enhanced therapeutic efficiency [11]. This approach highlights the potential of small-molecule self-assembled nanomedicines in overcoming the limitations of traditional delivery systems.

Immunotherapy is widely recognized as one of the most promising strategies in cancer treatment. However, the immunosuppressive tumor microenvironment (TME) significantly compromises the efficacy of immunotherapy by suppressing immune cell activity and promoting tumor immune escape [12,13]. Research has demonstrated that some chemotherapeutic agents, such as PTX, can induce immunogenic cell death (ICD), thereby enhancing anti-tumor immune responses [14]. Consequently, combined therapies integrating chemotherapy and immunotherapy often exhibit superior anti-tumor efficacy compared to monotherapy. For example, the ICD inducer Epirubinin (Epi) in combination with an immunomodulator (NLG919) has been shown to exert synergistic effects in tumor chemo-immunotherapy, with a tumor inhibition rate of 85.9 %, significantly higher than in the monotherapy group ($p < 0.001$) [15]. This highlights the potential of combining chemotherapeutics with immune adjuvants for stronger immune activation and improved therapeutic outcomes.

Resiquimod, a Toll-like receptor 7 and 8 (TLR7/8) agonist, effectively promotes the activation and maturation of antigen-presenting cells and enhances the release of pro-inflammatory cytokines and chemokines, leading to a stronger anti-tumor immune response [16]. Additionally, it can repolarize M2 macrophages into M1 macrophages, which helps reshape the tumor's immunosuppressive microenvironment [17,18]. However, the widespread distribution of free resiquimod *in vivo* may lead to non-specific immune responses and cause systemic toxicity and side effects [19–21]. To mitigate this issue, liposomes are employed for the targeted delivery of resiquimod *in vivo*.

In this study, we synthesized a phenylboronic acid-modified paclitaxel derivative (PTX-PBA) that can self-assemble into carrier-free nanoparticles in the presence of fructose or other monosaccharides and oligosaccharides. PTX-PBA-Fru NPs demonstrated enhanced antitumor efficacy and safety in 4T1 tumor-bearing mice compared to PTX injections. Additionally, when PTX-PBA-Fru NPs were combined with R848 liposomes, they achieved an impressive tumor inhibition rate of 93.71 % and a tumor eradication rate of 37.5 %.

2. Materials and methods

2.1. Regents and instruments

Paclitaxel (PTX, 98 %) and 1-(3-dimethylaminopropyl)-3-ethylcarbodiimide (hydrochloride) (EDCI) were bought from Meryer (Shanghai) Biochemical Technology Co., Ltd. (Shanghai, China). 4-Carboxyphenylboronic acid pinacol ester (4-CPBE) was purchased from Accela ChemBio Co., Ltd. (Shanghai, China). 4-Dimethylaminopyridine (DMAP) and sodium periodate ($NaIO_4$) were provided by Shanghai Aladdin Biochemical Technology Co., Ltd. (Shanghai, China). Sodium bicarbonate ($NaHCO_3$) and sodium chloride (NaCl) were obtained from Tianjin Beilian Fine Chemicals Development Co., Ltd. (Tianjin, China). Ammonium acetate (CH_3COONH_4) was purchased from Shanghai Macklin Biochemical Technology Co., Ltd. (Shanghai, China). Resiquimod (R848) was bought from Beijing MREDA Technology Co., Ltd. (Beijing, China). Soybean phospholipid (SPC) was acquired from Shenyang Tianfeng Biological Pharmaceutical Co., Ltd. (Shenyang, China). Cholesterol was provided by Shanghai Yuanye Bio-Technology Co., Ltd. (Shanghai, China). 3-(4,5-Dimethyl-2-thiazolyl)-2,5-diphenyl-2H-tetrazolium bromide (MTT) was acquired from Beijing Solarbio Technology Co., Ltd. (Beijing, China). Dichloromethane (DCM, super dry, with molecular sieves) was supplied by J&K Scientific Ltd. (Beijing, China). Acetonitrile and methanol (HPLC grade) were bought from Thermo Fisher Scientific Inc. (MA, USA). Deionized water was prepared by a Direct-D laboratory water purification system (Shanghai Yishuo Scientific Instruments Co., Ltd., China). The PTX and PTX-PBA injections used in this paper were prepared by dissolving PTX or PTX-PBA powder in a mixture of anhydrous ethanol and Cremophor EL (1:1, v/v), which was then diluted with normal saline.

^1H nuclear magnetic resonance (^1H NMR) spectra were acquired using a Bruker Avance-600 nuclear magnetic resonance spectrometer. For mass spectrometry analysis, measurements were performed on a G2-XS mass spectrometer (Waters, USA) equipped with an electrospray ionization source operating in negative ion mode. The mass scanning range was set to m/z 50–1500.

2.2. Cell line and animals

The 4T1 cell line was obtained from the National Infrastructure of Cell Line Resources (Beijing, China). Cells were cultured in RPMI 1640 medium supplemented with 10 % fetal bovine serum (FBS) and 1 % streptomycin-penicillin (Thermo Fisher Scientific) and maintained at 37 °C in a 5 % CO_2 incubator (Sanyo, Osaka, Japan). Female Balb/c mice, aged 6–8 weeks and weighing approximately 19 ± 1 g, were purchased from SPF (Beijing) Biotechnology Co., Ltd. (Beijing, China). Prior to experiments, the mice were acclimatized for one week under controlled conditions at 25 °C and 55 ± 5 % relative humidity. All animal experiments were conducted in compliance with the NIH (National Research Council) Guide for the Care and Use of Laboratory Animals and were approved by the Ethics Committee of the Institute of Medicinal Plant Development (approval number: SLXD-20230202013).

2.3. Synthesis of phenylboronic acid-modified paclitaxel derivative (PTX-PBA)

The synthesis of PTX-PBA involves two steps. The first step is to synthesize a 4-CPBE-modified PTX conjugate (PTX-PBE) through an esterification reaction [22]. Typically, 4-CPBE (161 mg, 0.65 mmoL), DMAP (12.2 mg, 0.10 mmoL), and EDCI (125 mg, 0.65 mmoL) were co-dissolved in 10 mL of anhydrous DCM and magnetically stirred at room temperature for 1 h in the dark. Subsequently, PTX (427 mg, 0.50 mmoL) was dissolved in an 8 mL anhydrous DCM and added to the system. Once PTX was completely consumed as indicated by thin layer chromatography (TLC) using a solvent system of DCM and acetone in a ratio of 8:1 (v/v), the mixture was transferred into a separatory funnel. The mixture was extracted with saturated $NaHCO_3$ and NaCl aqueous solution to remove EDCI and DMAP [23]. The organic phase was then collected, and DCM was evaporated under reduced pressure at 40 °C to yield a white solid powder of PTX-PBE (510 mg, 94 % yield). ^1H NMR (600 MHz, $CDCl_3$) δ 8.13–8.09 (m, 2H), 7.97 (d, J = 8.2 Hz, 2H), 7.89 (d, J = 8.2 Hz, 2H), 7.76 (dd, J = 7.8, 0.6 Hz, 2H), 7.65–7.61 (m, 1H), 7.54–7.49 (m, 3H), 7.44 (dd, J = 14.1, 5.8 Hz, 3H), 7.41 (dd, J = 7.8, 3.9 Hz, 3H), 7.33 (t, J = 7.3 Hz, 1H), 7.06 (d, J = 8.9 Hz, 1H), 6.28 (s, 1H), 6.26 (t, J = 9.2 Hz, 1H), 6.02 (dd, J = 8.9, 3.9 Hz, 1H), 5.71–5.63 (m, 2H), 4.97 (dd, J = 9.5, 1.7 Hz, 1H), 4.45 (ddd, J = 10.7, 6.5, 3.9 Hz, 1H), 4.31 (d, J = 8.4 Hz, 1H), 4.18 (d, J = 8.5 Hz, 1H), 3.81 (d, J = 7.1 Hz, 1H), 2.56 (ddd, J = 14.8, 9.6, 6.6 Hz, 1H), 2.50 (d, J = 3.8 Hz, 1H), 2.41 (s, 3H), 2.32 (dd, J = 15.2, 9.3 Hz, 1H), 2.23 (s, 3H), 2.13 (dd, J = 15.2, 8.9 Hz, 1H), 1.95 (s, 3H), 1.91–1.85 (m, 1H), 1.67 (s, 3H), 1.36 (s, 12H), 1.23 (s, 3H), 1.13 (s, 3H).

Secondly, the protective group of pinacol was removed from PTX-PBE to obtain PTX-PBA with an exposed boric acid group [24]. Specifically, PTX-PBE (510 mg, 0.47 mmoL) was dissolved in acetone (ACTN, 12 mL). An aqueous solution (6 mL) containing $AcONH_4$ (109 mg, 1.41 mmoL) and $NaIO_4$ (302 mg, 1.41 mmoL) was then added to the PTX-PBE solution. The mixture was stirred at room temperature in the dark for 36 h. Afterward, the organic phase was removed by evaporation in a vacuum at 40 °C. The resulting residue was collected by centrifugation at 8000 rpm for 10 min and subsequently dried at room temperature to obtain PTX-PBA, achieving a yield of 91 %. ^1H NMR (600 MHz, DMSO-d_6) δ 9.33 (d, J = 8.9 Hz, 1H), 8.38 (s, 2H), 8.02–7.88 (m, 6H), 7.86–7.82 (m, 2H), 7.70 (t, J = 7.4 Hz, 1H), 7.59 (t, J = 7.8 Hz, 2H), 7.57–7.52 (m, 3H), 7.48 (dd, J = 14.8, 7.6 Hz, 4H), 7.24 (t, J = 7.4 Hz, 1H), 6.30 (s, 1H), 5.87 (t, J = 8.8 Hz, 1H), 5.80 (q, J = 8.5 Hz, 1H), 5.54 (d, J = 8.7 Hz, 1H), 5.44–5.38 (m, 1H), 4.97 (d, J = 7.0 Hz, 1H), 4.92 (d, J = 10.9 Hz, 1H), 4.70 (s, 1H), 4.13 (dt, J = 11.0, 7.0 Hz, 1H), 4.04–3.96 (m, 2H), 3.61 (d, J = 7.2 Hz, 1H), 2.32 (dd, J = 14.5, 6.6 Hz, 1H), 2.29 (d, J = 19.3 Hz, 3H), 2.10 (s, 3H), 1.92–1.87 (m, 1H), 1.83 (s, 3H), 1.69–1.56 (m, 2H), 1.50 (s, 3H), 1.02 (s, 3H), 0.99 (s, 3H). The mass-to-charge ratio of $[M + CH_3COO]^-$ was found to be 1060.4958, which consisted of the theoretical value of 1060.38.

2.4. *HPLC methods*

The concentrations of PTX and PTX-PBA were measured using an HPLC system (DIONEX Ultimate 3000, USA) equipped with a Venusil XBP C18 (L) column (4.6 × 250 mm, 5 μm, Agela Technologies). The chromatographic system utilized a mobile phase consisting of acetonitrile, methanol, and water in a ratio of 50:15:35 (v/v/v) at a flow rate of 0.8 mL/min, with detection occurring at 227 nm. For the determination of R848, the same HPLC instrument was utilized, but with an Eclipse Plus C18 column (4.6 × 250 mm, 5 μm, Agilent Technologies). The method proceeded with a UV detector set to 248 nm and a mobile phase composed of methanol and a 0.1 % acetic acid aqueous solution in a ratio of 51:49 (v/v), at a flow rate of 0.8 mL/min.

2.5. *Metabolism of PTX-PBA in rat plasma or liver homogenate*

PTX-PBA injections were mixed with four volumes of rat blank plasma. This mixture was then incubated in a water bath at 37 °C. At specified time points, 50 μL samples were collected and mixed with 200 μL of anhydrous methanol (HPLC grade). The samples were vortexed for 30 s and sonicated for 1 min. After centrifugation at 10000 rpm for 15 min, the supernatant was analyzed using HPLC to determine the concentrations of PTX-PBA and PTX.

The liver homogenate was used to detect the *in vitro* biotransformation of PTX-PBA. Fresh livers from blank Balb/c female mice were cut into small chunks, rinsed with normal saline, and dried with absorbent paper. Then, 1 g of liver tissue was placed in a centrifuge tube, with 3 mL of normal saline and 5 small steel balls. This mixture was ground using a SCIENTZ-48 high-throughput tissue homogenizer. After centrifuging at 13000 rpm for 15 min, 10 mL of the supernatant was collected and mixed with 0.5 mL of PTX-PBA injections (0.94 mg/mL) for stirring at 37 °C. At specific time points, 200 μL of the sample solution was removed and mixed with 800 μL of anhydrous methanol. The mixture was vortexed for 30 s, sonicated for 1 min, and then centrifuged at 13000 rpm for 10 min. Finally, the supernatant was injected into HPLC to measure the concentrations of PTX-PBA and PTX.

2.6. *The mechanism of cytotoxicity of PTX-PBA*

The 4T1 cells were treated with 5 μg/mL of either PTX or PTX-PBA for 24 h. Tubulin was stained using Tubulin Tracker™ Green (Oregon Green™ 488 Taxol, bis-acetate, Cat. No. T34078) for 30 min, while the nucleus was stained with Hoechst 33342 for 15 min. Following these procedures, micrographs were captured using an ECLIPSE Ts2R fluorescent inverted microscope (Nikon, Japan).

2.7. *Preparation of PTX-PBA-Fru NPs and R848 liposomes*

PTX-PBA-Fru NPs can be prepared using the one-pot method. This involved mixing an anhydrous ethanol solution of PTX-PBA (50 mg in 5 mL) with a fructose aqueous solution (9 mg in 250 μL) at a molar ratio of 1:1. After mixing, the solution was diluted with 25 mL of deionized water. The resulting clear and opalescent nanoparticles were then evaporated in a vacuum at 40 °C to remove the ethanol and obtain the PTX-PBA-Fru NPs.

R848 liposomes (R848-Lipo) were prepared using the remote loading method described in references [25,26]. In summary, 24 mg of SPC, 8 mg of cholesterol, and 2 mg of DSPE-PEG2k-BPA were co-dissolved in 3 mL of anhydrous ethanol and evaporated at 45 °C to create a lipid thin film. This thin film was hydrated with 3 mL of a 250 mM ammonium sulfate solution. Following hydration, the mixture was sonicated in a water bath (250 W) for 10 min, then subjected to probe sonication for an additional 5 min to obtain the blank liposomes. The resulting liposomes were then dialysis in PBS solution for 24 h to remove ammonium sulfate from the external aqueous phase using dialysis bags with a molecular weight cut-off (MWCO) value of 8000–14000 Da. For the loading of R848, 2 mL of a R848 PBS solution was added to the 3 mL of blank liposomes and incubated at 50 °C for 1 h. The DSPE-PEG2k-BPA used in this formulation was synthesized in our laboratory from DSPE-PEG2k-NH_2 and pyridine-boric acid [27].

2.8. *The mechanism of self-assembly of PTX-PBA-Fru NPs*

Thin layer chromatography (TLC): In this analysis, an anhydrous ethanol solution of PTX-PBA (10 mg in 1 mL) and PTX (10 mg in 1 mL) was each thoroughly mixed with a fructose aqueous solution (1.8 mg in 50 μL) to create the mixtures PTX-PBA + Fru and PTX + Fru. TLC analysis was conducted using a developing solvent consisting of DCM and MeOH (8:1, v/v). The appearance of a new spot on the TLC plate observed using an Ultraviolet Analyzer at 254 nm indicated the formation of the PTX-PBA-Fru complex. Additionally, TLC analysis was performed on the PTX-PBA-Fru complex at different pH levels to investigate the pH-responsive dissociation of the complex.

^{11}B nuclear magnetic resonance spectra (^{11}B-NMR): Three samples were used for the ^{11}B-NMR analysis: (1) PTX-PBA/CD_3OD solution (10 mg dissolved in 1 mL), (2) the mixture at pH 7, consisting of the PTX-PBA/CD_3OD solution (10 mg in 1 mL) and fructose/D_2O solution (1.8 mg in 50 μL), (3) the mixture at pH 6, comprising the PTX-PBA/CD_3OD solution (10 mg in 1 mL) and fructose/D_2O solution (1.8 mg in 50 μL). The ^{11}B-NMR spectra for these samples were acquired using AVANCE III 600 MHz Nuclear Magnetic Resonance Spectrometer (Bruker, Germany), utilizing an artificial quartz nuclear magnetic tube (B < 0.01 ppm).

Quantum chemistry: The structures of the PTX-PBA, Fru, and PTX-PBA-Fru complexes were optimized using density functional theory (DFT) at the B97-3c [28] level, which includes the DFT-D3 dispersion correction and a short-range basis correction. To identify the optimal adsorption structures, one hundred potential complex structures were generated randomly and then screened using the Molclus program (Tian Lu, molclus program, Version 1.9.9.2). Each complex's clusters were initially optimized using the xTB program [29]. After this preliminary structural optimization, the cluster with the lowest energy was selected as the most probable adsorption structure. These selected clusters were further optimized at the B97-3c level. All calculations were performed using the ORCA 5.02 program [30,31]. The adsorption energy of the complex was calculated using the formula: $E\,(\text{absorb}) = E\,(A + B) - E\,(A) - E\,(B),$ where $E\,(A)$ and $E\,(B)$ are the energies of the isolated molecules, and $E\,(A + B)$ is the total energy of the complex structure. The basis set superposition error term was not calculated here, as the geometrical counterpoise correction (gCP) [32–34] has already been incorporated into the parameters of the B97-3c method. To analyze the intermolecular interactions, the Independent Gradient Model (IGM) [35] analysis was conducted using the Multiwfn program [36] to visualize the weak interactions. The results were then rendered using the Visual Molecular Dynamics (VMD) program [37].

2.9. *Characterization of PTX-PBA-Fru NPs and R848-Lipo*

Particle size: The mean particle size, polydispersity index (PDI), and zeta potential of PTX-PBA-Fru NPs and R848-Lipo were determined by a

Zetasizer Nano ZS (Malvern, United Kingdom), based on the principle of dynamic light scattering (DLS). Each sample was measured in triplicate.

Drug loading content: The drug loading content (DLC) was calculated by the formula: DLC (%) = We/Wt × 100%. In detail, 5 mL of R848-Lipo was freeze-dried to obtain solid powder. 10 mg of the obtained powder was accurately weighted to represent the total weight of the drug-loaded liposomes (Wt) and dissolved in 2 mL of methanol. The mixture was then centrifuged at 8000 rpm for 10 min, and the diluted supernatant was analyzed by HPLC to determine the concentration of R848. This allowed for the calculation of the weight of R848 encapsulated in the 10 mg of lyophilized powder (We).

Encapsulation efficiency: The encapsulation efficiency (EE) was calculated using the formula: EE (%) = (1 − Cf /Ct)*100%. To determine this, 0.4 mL of R848-Lipo was centrifuged in an ultrafiltration centrifuge tube with a MWCO of 3 kDa at 8000 rpm for 15 min. The filtrate collected at the bottom of the tube was then analyzed by HPLC to determine the concentration of free R848 (Cf). Additionally, 0.1 mL of R848-Lipo was mixed with 0.9 mL of chromatographic methanol, and the resulting mixture was sonicated for 1 min. This was followed by centrifugation at 10000 rpm for 10 min. The supernatant obtained was analyzed by HPLC to measure the concentration of total R848 (Ct), which was used to calculate the EE.

Transmission Electron Microscope (TEM) observation: 10 μL of PTX-PBA-Fru NPs and R848-Lipo were each dropped on a copper grid with an ultra-thin carbon film. After allowing the samples to air-dry for 10 min, the excess liquid was removed. R848-Lipo was then stained with a 3 % (w/v) uranyl acetate solution. The morphology of both PTX-PBA-Fru NPs and R848-Lipo was examined using a Tecnai G2 F30 S-TWIN transmission electron microscope (FEI Company, US).

X-ray crystal diffraction (XRD) analysis: XRD analysis was conducted to obtain X-ray diffraction patterns of various samples, including PTX-PBA solid powder, bulk fructose powder, the lyophilized powder of PTX-PBA-Fru NPs, and a physical mixture of PTX-PBA and fructose at a mass ratio of 10:1.8. The analysis was performed using a D8 ADVANCE X-ray diffractometer (Bruker, Germany). For the wide-angle diffraction testing, the tube current was set to 40 mA, and the tube voltage was maintained at 40 kV. The scanning angle varied from 5° to 80° at a rate of 5° per minute.

The stability in physiological media: The stability of PTX-PBA-Fru NPs and R848-Lipo was assessed by mixing them with equal volumes of 1.8 % normal saline (m/v), 10 % glucose solution (m/v), or with four volumes of phosphate-buffered saline (PBS, pH 7.4), fetal bovine serum (FBS) or plasma. These mixtures were incubated at 37 °C. The particle sizes of the mixtures were recorded at 0, 2, 4, 6, 8, and 12 h. Additionally, any changes in physical appearance changes, such as aggregation and precipitation, were observed to evaluate the stability of the PTX-PBA-Fru NPs and R848-Lipo in physiological media.

2.10. *In vitro drug release behavior of PTX-PBA-Fru NPs*

PTX-PBA-Fru NPs (1 mg/mL, 1.5 mL) were placed in a dialysis bag with a MWCO of 100 kDa and dialyzed against 100 mL of 5 % glucose solution containing 1.0 % Tween 80 (m/v) at pH 6.5 and pH 7.2. Dialysis was carried out at 37 °C with a stirring speed of 150 rpm. At predetermined time intervals, 500 μL of the release medium was collected, and an equal volume of fresh pre-warmed (37 °C) release medium was immediately replenished. The collected samples were mixed with 0.5 mL of methanol (HPLC grade) and centrifuged at 10,000 rpm for 10 min. The supernatant was then analyzed using HPLC to quantify the concentrations of PTX and PTX-PBA. The release medium was replaced with fresh medium every 24 h. The experiment was performed in triplicate.

2.11. *In vitro cytotoxicity assay*

4T1 cells (8×10^3 cells/well, 200 μL) were seeded in 96-well plates and incubated at 37 °C in a 5 % CO_2 atmosphere for 24 h. After removing the complete medium, PTX injections, PTX-PBA injections, *p*-carboxyphenylboronic acid (PBA) and PTX-PBA-Fru NPs were diluted with incomplete medium to various concentrations and added to the wells. The PBA solution was prepared using the same method as the PTX injections. The plates were then incubated for 72 h, with blank medium serving as the control. Following incubation, 20 μL of MTT solution (5 mg/mL in PBS) was added to each well and incubated for an additional 4 h. The medium was then removed, and 200 μL of DMSO was added to each well to dissolve the formazan crystals. The absorbance of each well was measured at 570 nm using a multi-mode microplate reader (Tecan, Switzerland). Cell viability was calculated using the formula: Cell viability rate (%) = $OD_{treatment}/OD_{control}$*100%, where $OD_{treatment}$ represents the absorbance of drug-treated wells and $OD_{control}$ represents the absorbance of wells treated with incomplete medium. The half inhibitory concentration (IC50) was determined using GraphPad Prism 8 (GraphPad Software, Boston, USA).

2.12. *In vivo anti-tumor efficacy and ICD induction of PTX-PBA-Fru NPs*

Anti-tumor evaluation: Tumor-bearing mice were established by subcutaneously injecting 4T1 cells (suspended in RPMI 1640 medium at a concentration of 2.0×10^6 cells in 0.2 mL) into the right armpit of female Balb/c mice. Once the tumors reached an average volume of approximately 100 mm^3, the mice were randomly divided into four groups (n = 6) and received intravenous injections every other day for seven treatments. The groups received the following treatments: normal saline (NS, the negative control group, 0.2 mL), PTX injections (8 mg/kg, the positive control group, 0.2 mL), PTX-PBA injections and PTX-PBA-Fru NPs (9.4 mg/kg, corresponding to 8 mg/kg PTX, 0.2 mL).

Tumor volume was measured using the formula: $V\left(mm^3\right) = a \times b^2/2$, where a is the long diameter of the tumor and b is the short diameter. The body weight was measured every two days. When the mice were at the end of the study, blood was collected from the eyeball into clean centrifuge tubes and stored at 4 °C for 4 h. The samples were centrifuged at 3500 rpm for 10 min to isolate serum. Serum levels of alanine aminotransferase (ALT) and aspartate aminotransferase (AST) were measured using an automated biochemical analyzer (AU480, Beckman Coulter, Japan). Additionally, serum sialic acid (SA) levels were quantified using a Sialic Acid Assay Kit (GRACE, China) to assess the potential for inhibiting tumor growth and metastasis. Following this, tumors and major organs, including the heart, liver, spleen, lungs, and kidneys, were collected and weighed for further analysis. The tumor inhibitory rates (TIR) were calculated using the formula: $TIR = \left(1 - W_{experiment}/W_{control}\right) \times 100\%$, where $W_{control}$ and $W_{experiment}$ refer to the mean tumor weights of the NS group and the experimental groups, respectively. The corresponding organ indexes were also calculated by dividing the organ weight by the total body weight of the mice.

ICD biomarkers analysis: ICD biomarker analysis: Serum levels of high mobility group protein B1 (HMGB-1) were measured using an HMGB-1 ELISA kit (Beijing Chenglin Biotechnology Co., Ltd., Catalog #AD2598Mo). For adenosine triphosphate (ATP) detection, 5×10^4 4T1 cells were seeded in 24-well plates. After 24 h, the culture medium was replaced with either NS, PTX injections, PTX-PBA injections, or PTX-PBA-Fru NPs at a concentration of 10 μg/mL, followed by another 24-h incubation. The supernatants were collected, and ATP levels were quantified using an ATP Content Assay Kit (spectrophotometric method, Pyeast Bio. Co., Ltd., Catalog #SW1092) according to the manufacturer’s instructions.

2.13. *In vitro dendritic cell activation*

Immature bone marrow-derived dendritic cells (BMDCs) were isolated from the femurs and tibiae of female C57BL/6J mice [38,39]. Briefly, the cleaned bones were disinfected by submerging in 70 % ethanol for 5–10 s and then transferred to a sterile bench, where they were washed with ice-cold PBS. Both ends of the bones were cut as close to the joint as possible. A syringe filled with cold PBS was used to flush out the bone marrow into a petri dish placed on ice. The rinsing process was repeated 2–3 times until the bones turned completely white. The cell suspension was then filtered through a 70 μm strainer to remove any clumps. Red blood cells were lysed using a red blood cell lysis buffer, followed by centrifugation at 1500 rpm for 5 min. The isolated BMDCs were resuspended in 10 mL of RPMI complete medium supplemented with 20 ng/mL mouse GM-CSF recombinant protein (GM-CSF, PeproTech) and seeded at a density of 1×10^6 cells per dish. The cells were cultured in a 5 % CO_2 incubator at 37 °C. On day 3, an additional 10 mL of RPMI complete medium containing 20 ng/mL GM-CSF was added to the dishes. On day 5, 10 mL of the medium was removed, centrifuged, and re-suspended in 10 mL of fresh RPMI complete medium containing 20 ng/mL GM-CSF before being returned to the original dish. On day 7, BMDCs were harvested and co-cultured with 4T1 cells at a density of 4×10^5 BMDCs per well and 4×10^4 4T1 cells per well in 12-well plates.

The co-culture systems were treated with NS, PTX injections (2 μg/mL), PTX-PBA-Fru NPs (2.35 μg/mL, equivalent to 2 μg/mL of PTX), R848 solution (0.5 μg/mL, dissolved in NS) and a combination of PTX-PBA-Fru NPs and R848-Lipo (2.35 μg/mL of PTX-PBA and 0.5 μg/mL of R848) for 12 h. After treatment, the cells were collected and stained with the following antibodies: CD45 monoclonal antibody (PerCP-Cyanine5.5, eBioscience), PE anti-mouse CD11c, FITC anti-mouse CD80, and APC anti-mouse CD86 (Proteintech). Staining was performed for 30 min at room temperature in the dark. Subsequently, 1 mL of cell staining buffer (CSB) was added to the cells, which were then washed and centrifuged at 3500 rpm for 5 min. The cells were resuspended in 0.2 mL of CSB and analyzed using flow cytometry (CytoFLEX LX, BECKMAN COULTER).

2.14. *Macrophage polarization and re-education*

Bone marrow-derived macrophages (BMDMs) were isolated from female C57BL/6 mice using the same protocol as for BMDCs. To obtain M0 macrophages, BMDMs were cultured in RPMI complete medium supplemented with 10 ng/mL mouse M-CSF recombinant protein (eBioscience) for 7 days. The cells were then collected and seeded into 12-well plates at a density of 4×10^5 cells per well. To induce the M1 phenotype, lipopolysaccharide (LPS, Solarbio) was added at 200 ng/mL for 12 h. For M2 polarization, recombinant murine interleukin-4 (IL-4, PeproTech) was applied at 20 ng/mL for 12 h [17]. After polarization, M2 macrophages were treated with NS, PTX injections (2 μg/mL), PTX-PBA-Fru NPs (2.35 μg/mL), R848 solution (0.5 μg/mL), or PTX-PBA-Fru NPs combined with R848-Lipo (2.35 μg/mL of PTX-PBA and 0.5 μg/mL of R848) for an additional 12 h.

Following treatment, the cells were collected and suspended in PBS. They were stained with the Zombie Violet™ Fixable Viability Kit (BV421, BioLegend) at room temperature in the dark for 15 min. After washing with CSB and centrifugation at 3500 rpm for 5 min, the cells were then resuspended in CSB and incubated with purified anti-mouse CD16/32 antibody (Elabscience) for 15 min. Next, the cells were stained with APC anti-mouse CD45 (Proteintech), F4/80 monoclonal antibody (PerCP-Cyanine5.5, eBioscience), and PE anti-mouse CD86 (Proteintech) for 30 min. After another wash and centrifugation, the cells were resuspended in CSB and fixed for 10 min with 0.5 mL of pre-cooled fixation buffer (Shanghai Yuanye Bio-Technology Co., Ltd.) at room temperature. Following centrifugation at 3500 rpm for 5 min, the supernatant was discarded. The cells were then incubated with 1 mL of permeabilization buffer for 15 min, after which they were centrifuged and re-suspended in CSB. FITC anti-mouse CD206 antibody (Proteintech) was added for incubation at room temperature for 30 min in the dark. Finally, the cells were washed with CSB, centrifuged, and re-suspended in 0.2 mL of CSB for flow cytometry analysis.

2.15. *In vivo anti-tumor efficacy of chemoimmunotherapy*

To further investigate the synergistic effect of PTX-PBA-Fru NPs combined with immunotherapy, R848 liposomes were co-administered as immune adjuvants, and the survival curves were evaluated. 4T1 tumor-bearing mice were divided into seven groups ($n = 8$) to receive intravenous injections every other day for 14 days as follows: (1) normal saline (NS), (2) PTX injections (16 mg/kg), (3) PTX-PBA injections (18.8 mg/kg, equivalent to 16 mg/kg of PTX), (4) PTX-PBA-Fru NPs (18.8 mg/kg, equivalent to 16 mg/kg PTX), (5) R848 solution (1.5 mg/kg, prepared in NS), (6) PTX-PBA injections + R848-Lipo, and (7) PTX-PBA-Fru NPs + R848-Lipo (18.8 mg/kg for PTX-PBA and 1.5 mg/kg for R848). It is important to note that the R848-Lipo was administered intravenously 24 h after the PTX or PTX-PBA injections. During the treatment period, tumor volume and body weight were continuously monitored. On day 14, blood was taken from the orbits of three mice in each group to collect serum for the levels of IL-12 and TNF-α using ELISA kits from Beijing MREDA Technology Co., Ltd., following the manufacturer's protocol.

Mice were considered dead when their tumor volume approached 2000 mm^3. The survival curves and median survival times were analyzed using GraphPad Prism software. On day 105, 2×10^6 4T1 tumor cells were re-injected subcutaneously into the right axilla of mice whose tumors had completely subsided, with no further treatment administered. Tumor size and body weight measurements continued until day 126.

2.16. *In vivo immune activation*

Another cohort of 4T1 tumor-bearing mice was treated with NS, PTX injections, PTX-PBA-Fru NPs, R848 solution, and a combination of PTX-PBA-Fru NPs with R848-Lipo, following the same treatment regimen described in the "In vivo anti-tumor efficacy of chemoimmunotherapy" section. After seven administrations, three mice from each group were selected for tumor and spleen analysis. The proportions of $CD3^+$, $CD4^+$, and $CD8^+$ T cells, as well as the ratio of M2-type to M1-type macrophages in the tumors, were analyzed using flow cytometry. Immunofluorescence staining was performed to visualize the expression of iNOS (an M1 marker) and CD206 (an M2 marker) in tumor tissues. Additionally, spleens collected to evaluate the levels of memory T cells.

Analysis of tumor immune microenvironment: Approximately 0.5 g of tumor tissue was placed into an EP tube and minced into small pieces using scissors. Next, 500 μL of collagenase II and 500 μL of collagenase IV (Biosharp) were added, along with 2 mL of DNase (BioFROX) and 2 mL of RPMI 1640 medium. The mixture was digested at 37 °C for 40 min. After digestion, the sample was filtered through a 250-mesh nylon screen, and the filtrate was centrifuged at $500\times g$ for 10 min. The supernatant was discarded, and the resulting single-cell suspension (100 μL, 10×10^6 cell/μL) was diluted in CSB. Subsequently, 1 μL of anti-mouse CD16/32 antibody was added, and the mixture was incubated for 5 min. Zombie dye was added according to the manufacturer's recommended dosage, followed by a 10-min incubation. Then, 1 mL of PBS was added, and the sample was centrifuged at 1500 rpm for 5 min. The supernatant was discarded, and the cells were re-suspended in CSB.

The following antibodies were added at their recommended dosages: APC/Cyanine7 anti-mouse CD45, PerCP/Cyanine5.5 anti-mouse CD3, FITC anti-mouse CD4, PE-Cy7 anti-mouse CD8, BV421 anti-mouse F4/80, BV605 anti-mouse CD11b, and APC anti-mouse CD86 (all from BioLegend). The samples were incubated for 15 min. After incubation, 1 mL of 1 × lysing buffer (BD Biosciences) was added, and the mixture was incubated for an additional 10 min. The samples were then centrifuged, and the supernatant was discarded. Next, 250 μL of fixation buffer was added and incubated for 20 min. After incubation, 1 mL of CSB was added, and the samples were centrifuged again. Subsequently, 1 mL of permeabilization buffer was added for 5 min. Following centrifugation, PE anti-mouse CD206 antibody was added for staining. After 30 min of incubation, 1 mL of CSB was added, and the samples were centrifuged once more. The supernatant was removed, and the cells were resuspended in 200 μL of CSB for flow cytometry analysis using a CytoFLEX LX instrument (BECKMAN COULTER).

Immune memory analysis: The spleen was ground in 1 mL of 1640 medium. After centrifugation, the cells were re-suspended at 1×10^7 cells/mL. Zombie dye was added to 100 μL of the single-cell suspension for staining. After a 10-min incubation, the cells were centrifuged again, and the following antibodies were added for 15 min: APC/Cyanine7 anti-mouse CD45, PerCP/Cyanine5.5 anti-mouse CD3, PE-Cyanine7 anti-mouse CD44, and PE anti-mouse CD62L. After another centrifugation, the cells were re-suspended in 200 μL of PBS for flow cytometry analysis.

2.17. Safety evaluation

Systemic anaphylaxis protocols: The experimental protocols for systemic anaphylaxis were adapted from the literature [40] with modifications. Female Balb/c mice were randomly divided into three groups and administered intravenously with (1) NS, (2) PTX injections (16 mg/kg), or (3) PTX-PBA-Fru NPs (18.8 mg/kg, equivalent to 16 mg/kg of PTX) on days 0, 2, 4 and 6 for a total of four doses (0.2 mL per mouse, n = 6). On the sixth day, after the fourth dose, an Evans blue solution (0.5 mg/mL in NS) was injected into the tail veins of the mice at a volume of 0.1 mL to evaluate vascular permeability. The overall color change in the mice's bodies was observed. Additionally, the general condition and allergic symptoms of the mice were monitored before and after administration, along with measurements of anal temperatures.

Maximum tolerated dose (MTD) determination: The MTDs for PTX injections and PTX-PBA-Fru NPs were evaluated in healthy Balb/c mice. Six animals (three males and three females per group) were administered either PTX injections at doses of 30, 40, or 50 mg/kg, PTX-PBA-Fru NPs at doses of 50, 100, 150, 200, or 400 mg/kg, or NS intravenously on days 0, 4, and 8. The mice's behavior and body weight changes were monitored daily. Dosing was discontinued if mortality occurred or if a 10 % weight loss was observed after administration. At the end of the experiment, organs were dissected and examined for significant damage. The MTD was defined as the highest dose that did not cause mortality, resulted in less than a 10 % weight loss, and did not induce significant organ damage in the mice.

2.18. Statistical analysis

NMR spectra were analyzed using the MestReNova software (Mestrelab Research, S.L., Spain). All data were statistically analyzed with IBM SPSS Statistics software, Version 26 (IBM Corporation, Armonk, NY, USA). For comparisons between multiple groups, one-way analysis of variance (ANOVA) was employed when the data followed a normal distribution, the Kruskal-Wallis and Median test were applied for non-normally distributed data. The independent samples *t*-test was used to compare the statistical differences between the two groups of data. A p-value of less than 0.05 was considered statistically significant.

3. Results and discussion

3.1. Synthesis and characterization of PTX-PBA

The synthesis of PTX-PBA was illustrated in Fig. 1A. The purity of the synthesized PTX-PBA exceeded 95 %, as determined by HPLC using the area normalization method. The ^{1}H NMR spectra of PTX-PBE and PTX-PBA, compared to that of PTX, were presented in Fig. S1. As shown, the peak at δ 1.36 ppm corresponded to the 12 methyl hydrogens of pinacol, and the absence of a signal for carboxyl hydrogens in the range of δ 10–12 ppm indicated the successful synthesis of PTX-PBE. In the PTX-PBA spectrum, the disappearance of the pinacol methyl hydrogens confirmed successful deprotection. Additionally, the exact mass of PTX-PBA was calculated to be 1001.36 ($C_{54}H_{56}BNO_{17}$). The molecular ion peak at *m/z* 1060.4958 in the mass spectrum (Fig. S2) corresponded to PTX-PBA plus an acetate ion $[M + CH_3COO]^-$. In summary, these results confirm the successful synthesis of PTX-PBA.

The HPLC analysis of PTX and PTX-PBA was presented in Fig. S3. The separation factor exceeded 1.5, meeting the requirements for qualitative analysis. The recovery rate ranged from 98 % to 101 %, indicating

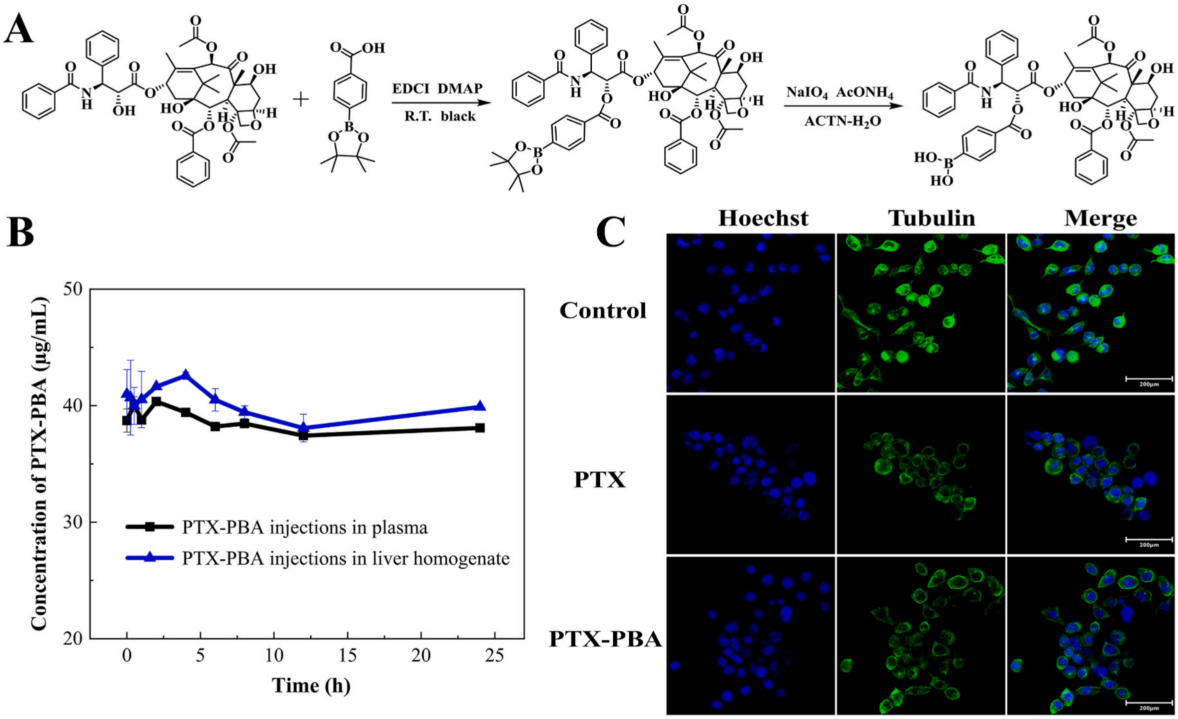

Fig. 1. Synthesis and characterization of PTX-PBA. (A) The synthetic route for PTX-PBA. (B) Drug concentrations of PTX-PBA incubated in rat blank plasma or liver homogenate (n = 3, mean ± SD). (C) PTX-PBA disrupted microtubule arrangement, inhibited mitosis, and induced cell apoptosis (scale bar, 200 μm).

excellent reliability. Both repeatability and intermediate precision showed a low relative standard deviation (RSD) of less than 5 %. The standard curve equations were as follows: $y = 1.032x + 0.6189$ ($R^2 = 0.9994$, 0.05–100 μg/mL) for PTX; $y = 0.9903x - 0.0277$ ($R^2 = 0.9992$, 0.05–50 μg/mL) for PTX-PBA; and $y = 1.5604\,x - 0.5074$ ($R^2 = 0.9996$, 0.01–500 μg/mL) for R848.

As shown in Fig. 1B, the concentration of PTX-PBA remained nearly constant in both rat plasma and liver homogenate, with no detectable levels of PTX. This observation suggested that PTX-PBA underwent minimal metabolism in plasma or liver homogenate. Previous studies have reported that modifying the 2′-OH of PTX resulted in a prodrug that releases free PTX *in vivo* [41,42]. However, PTX-PBA behaved differently from the compounds described in the literature. This discrepancy may be attributed to the steric effects of phenylboronic acid or the affinity of PTX-PBA to plasma proteins, which may hinder the accessibility of esterase [43].

To investigate the effects of PTX-PBA on microtubules in living cells, we used Tubulin Tracker to observe changes in microtubule integrity and structure [44]. As shown in Fig. 1C, normal 4T1 cells in the control group exhibited a well-organized microtubule network, which is essential for maintaining cell morphology. In contrast, cells treated with PTX and PTX-PBA showed reduced tubulin levels, with microtubules adhering to the nucleus and displaying a disordered arrangement. Notably, compared to the control group, cells treated with PTX and PTX-PBA appeared more rounded, with enlarged nuclei and intense staining due to chromatin condensation associated with apoptosis. In summary, although PTX-PBA is not a prodrug, it functions similarly to PTX by disrupting tubulin assembly homeostasis, inhibiting mitosis, effectively suppressing cell proliferation, and promoting apoptosis.

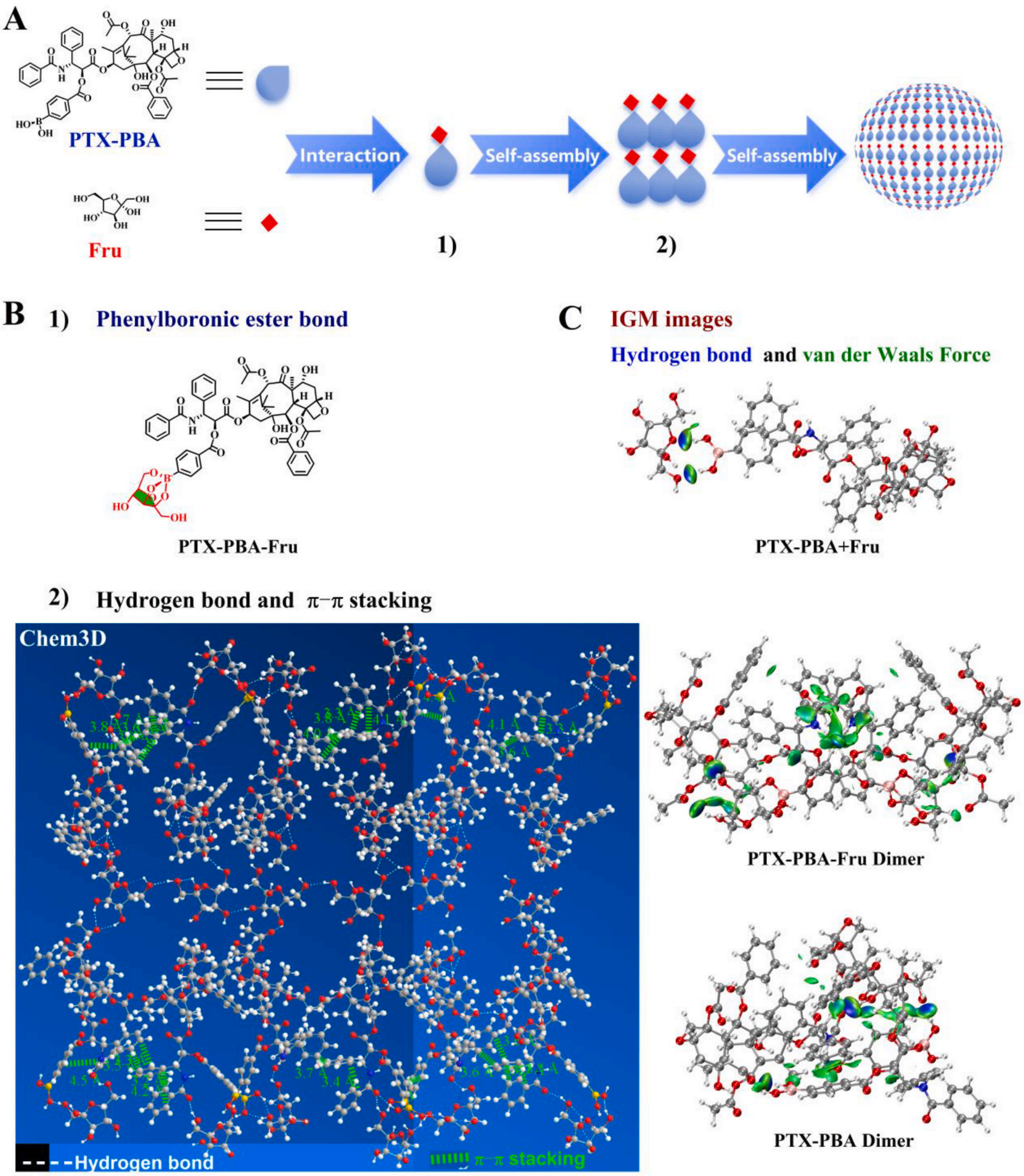

Fig. 2. Mechanism of self-assembly of PTX-PBA-Fru NPs. (A) Schematic representation of the self-assembly process of PTX-PBA-Fru NPs. (B) Driving forces behind self-assembly: 1) The pH-responsive dynamic borate ester bond (verified by TLC and ^{11}B-NMR); 2) Hydrogen bonds formed between PTX-PBA and PTX-PBA/Fru, as well as the π-π interactions between PTX-PBA molecules, simulated using Chem 3D. (C) Weak interactions among PTX-PBA + Fru, PTX-PBA-Fru dimer, and PTX-PBA dimer were analyzed using the Independent Gradient Model (IGM).

3.2. The mechanism of self-assembly of PTX-PBA-Fru NPs and its pH-responsive disassociation

The schematic diagram illustrating the self-assembly process is presented in Fig. 2A. The results from TLC, shown in Fig. S4A, indicated that PTX combined with Fru did not form a complex, as both PTX and the PTX + Fru mixture exhibited the same Rf value. In contrast, the combination of PTX-PBA and Fru produced a distinct spot, differing from those of PTX-PBA and Fru alone (which showed no ultraviolet absorption at 254 nm). This suggested the formation of a new compound, referred to as the PTX-PBA-Fru complex.

The PTX-PBA-Fru complex demonstrated considerable stability at pH 7. However, it rapidly dissociated into PTX-PBA at pH 6. When the pH was readjusted to 7 (Fig. S4B), the complex reformed again, indicating that the PTX-PBA-Fru complex exhibits pH-responsive properties for its association and dissociation. Notably, when the pH of the PTX-PBA-Fru NPs was adjusted from 6.5 to pH 6, a significant amount of PTX-PBA precipitated immediately, as PTX-PBA is insoluble in water after nanoparticle dissociation.

Additionally, ^{11}B-NMR analysis revealed that free PTX-PBA exhibited a distinct B peak at δ 2.66 ppm (Fig. S5). Upon mixing the PTX-PBA/CD_3OD solution with an aqueous fructose solution, the B peak shifted to δ 31.23 ppm, indicating the formation of a covalent bond between PTX-PBA and fructose. When the mixture was adjusted to pH 6, the spectrum displayed a chemical shift similar to that of PTX-PBA, suggesting that the covalent bond was broken under acidic conditions. Therefore, the bond formed between PTX-PBA and fructose is identified as a pH-responsive dynamic borate ester bond [45], as illustrated in Fig. 2B–1.

PTX-PBA alone failed to form nanoparticles under similar conditions, indicating that fructose is an essential component for the formation of PTX-PBA-Fru NPs. The interaction between PTX-PBA and Fru was further analyzed using Chem 3D simulations and quantum chemistry. As shown in Fig. 2B–2, PTX-PBA and fructose were cross-linked through hydrogen bonds and π-π interactions. To compare the strength of

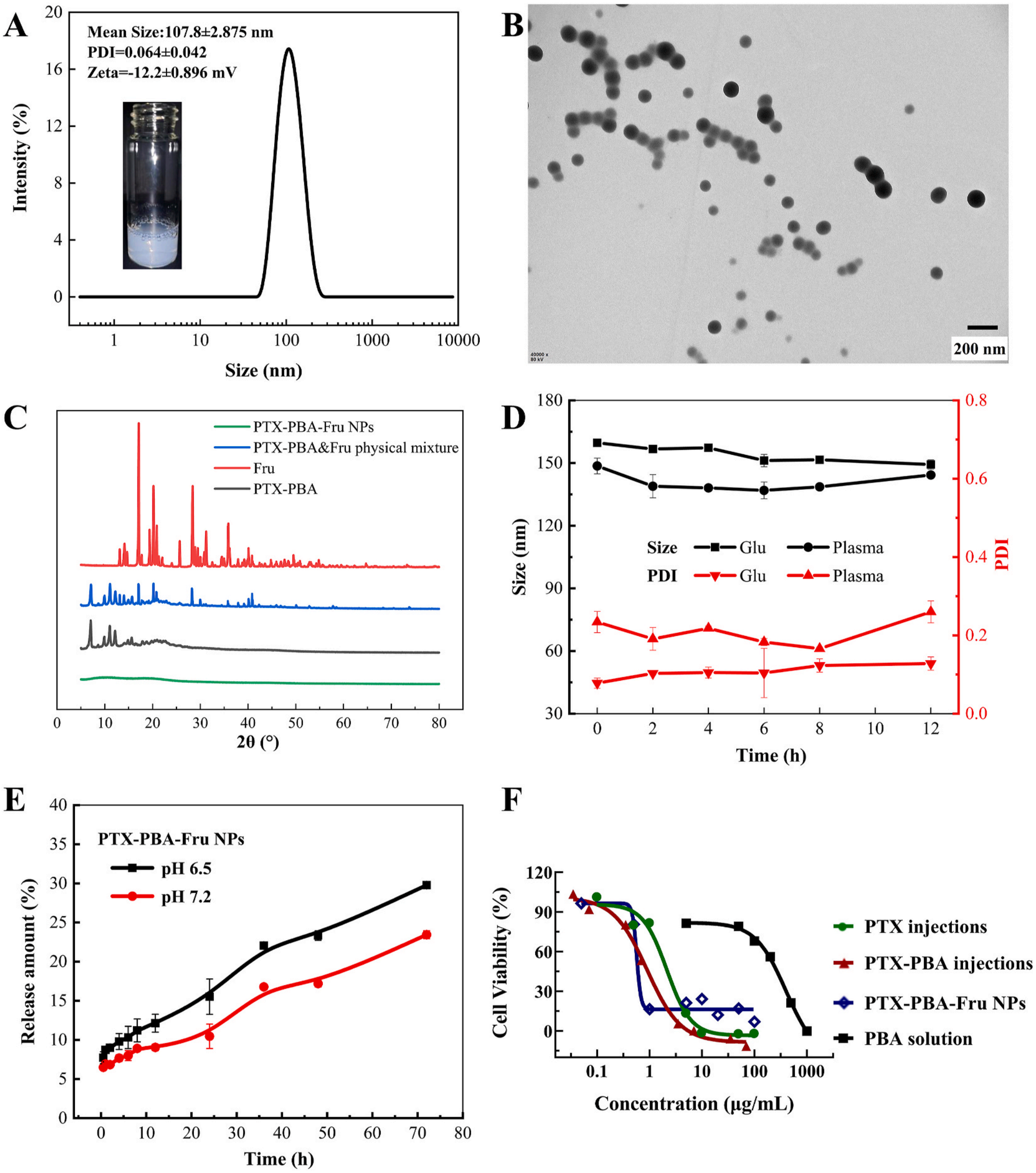

Fig. 3. Characterization of PTX-PBA-Fru NPs. (A) Particle size distribution and (B) TEM image of PTX-PBA-Fru NPs (scale bar, 200 nm). (C) XRD patterns of PTX-PBA bulk powder, fructose granules, physical mixture, and the lyophilized powder of PTX-PBA-Fru NPs. (D) The particle size and PDI value of PTX-PBA-Fru NPs in 5 % glucose and plasma (n = 3, mean ± SD). (E) The drug release behavior of PTX-PBA-Fru NPs (n = 3, mean ± SD). (F) *In vitro* cytotoxicity of PTX injections, PTX-PBA injections, PTX-PBA-Fru NPs and PBA solution against 4T1 cells over 72 h.

adsorption, we examined the adsorption energy. A negative value indicates an exothermic process, with a smaller value suggesting stronger adsorption and greater stability of the adsorbed system. In contrast, a positive value indicates that adsorption is thermodynamically unfavorable. As shown in Table S1, the adsorption energy of the PTX-PBA-Fru dimer was −2.06 eV, which is lower than that of the PTX-PBA and fructose combination, as well as the PTX-PBA dimer. This suggested that the PTX-PBA-Fru dimer exhibits greater stability. Additionally, PTX-PBA can form dimers with an adsorption energy of −1.55 eV, while complexes formed between PTX-PBA and fructose alone were unstable, with an adsorption energy of −0.20 eV.

Although intermolecular interactions obtained through IGM simulation (Fig. 2C) revealed that both the PTX-PBA-Fru complex and PTX-PBA could self-aggregate into dimers via intermolecular hydrogen bonds (e.g., B-O-H···O=C, C-O-H···O=C) and van der Waals forces, further aggregation was unlikely once the dimers formed. This is because no additional hydrogen bond donors are available to facilitate further aggregation. The polyhydroxy structure of fructose can serve as a bridge for hydrogen bonds, promoting further aggregation between multiple molecules or dimers to form PTX-PBA-Fru NPs.

3.3. Characterization of PTX-PBA-Fru NPs and R848-Lipo

As shown in Fig. 3A, PTX-PBA-Fru NPs exhibited a mean particle size of 107.8 ± 2.9 nm, a PDI value of 0.064 ± 0.042, and a zeta potential of −12.2 ± 0.9 mV. TEM images revealed a spherical morphology of the nanoparticles (Fig. 3B). XRD patterns indicated that PTX-PBA, fructose, and their physical mixture exhibited crystal diffraction peaks (Fig. 3C). In contrast, the XRD pattern of PTX-PBA-Fru NPs showed no diffraction peaks, suggesting that the crystalline structure transformed into an amorphous state due to interactions between fructose and PTX-PBA.

Furthermore, various monosaccharides (e.g., glucose, D-fructose 1,6-bisphosphate trisodium salt, mannose), and disaccharides (e.g., isomaltulose), trisaccharides (e.g., kestose), tetrasaccharides (e.g., nistose trihydrate), and the polyphenolic compound salvianolic acid B were tested. All these substances were capable of self-assembling into nanoparticles with PTX-PBA under the same conditions (Table S2). Among the tested nanoparticles, PTX-PBA-Fru NPs demonstrated the best storage stability, with negligible particle size enlargement over 3 days. In contrast, salvianolic acid B exhibited the poorest stability, maintaining its original particle size for only 3 h. It had been reported that fructose, among various monosaccharides, had the highest affinity to form complex with the boric acid group, with the furan ring being the dominant configuration [46]. Equal molar amounts of PTX-PBA and fructose were used to fabricate PTX-PBA-Fru NPs, resulting in a high theoretical drug loading capacity of 84.7 %.

As illustrated in Fig. S6, R848-Lipo displayed an average particle size of 95.22 ± 2.01 nm, a PDI of 0.279 ± 0.015, and a zeta potential of −18.5 ± 0.5 mV, with a morphology consistent with lipid bilayers. The liposome exhibited an impressive encapsulation efficiency of 83.6 %. The actual drug loading content of R848-Lipo was calculated to be 5.08 %, which is close to the theoretical drug loading content of 5.56 %.

PTX-PBA-Fru NPs remained stable at room temperature for three days, as shown in Table S3, with only minimal changes in mean particle size. We also attempted to freeze-dry the nano-preparation for long-term storage. However, the resulting freeze-dried powder could not be directly dispersed in water. Instead, it had to be dissolved in ethanol and then diluted with water to reconstitute the nanoparticles. When PTX-PBA-Fru NPs were incubated with NS or PBS, precipitation occurred immediately, indicating that PTX-PBA-Fru NPs are unstable in these solutions. In contrast, PTX-PBA-Fru NPs exhibited good stability in a 5 % glucose solution and plasma for at least 12 h, with no significant changes in mean particle size or PDI values (Fig. 3D). This suggested that PTX-PBA-Fru NPs should be freshly prepared in a 5 % glucose solution for *in vivo* drug delivery, as the relatively high ionic strength of NS or PBS may compromise their stability.

Further investigation into dilution stability revealed that 100 μg/mL, 10 μg/mL, and 1 μg/mL concentrations of PTX-PBA-Fru NPs could be achieved by diluting 1 mg/mL nanoparticles in 5 % glucose. As indicated in Table S3, the 100 μg/mL and 10 μg/mL samples exhibited small mean particle sizes and narrow size distributions over three days, indicating good dilution stability. However, the 1 μg/mL sample showed no detectable nanoparticles, behaving similarly to deionized water, which aligns with the saturated solubility of PTX-PBA in water (4.07 μg/mL).

Similar to other drug-loaded liposomes, R848-Lipo demonstrated stability in various physiological media, including 0.9 % NaCl, PBS, 5 % glucose, and FBS (Fig. S7). There were minimal changes in particle size or PDI values, and no precipitation or aggregation was observed, indicating its suitability for intravenous administration.

3.4. In vitro drug release behavior of PTX-PBA-Fru NPs

As shown in Fig. 3E, PTX-PBA-Fru NPs exhibited a sustained drug release profile, with a slightly faster release rate at pH 6.5 compared to pH 7.2. The *in vitro* release data for PTX-PBA-Fru NPs covers only 3 days because the self-assembled nanoparticles inherently lack long-term stability and can maintain their structure for no more than 3 days before precipitation. PTX-PBA-Fru NPs, prepared using pure water, had a natural pH of approximately 6.5. When the pH was adjusted to 5, PTX-PBA-Fru NPs quickly precipitated due to the decomposition of the borate ester bond between PTX-PBA and Fru. However, when the pH is adjusted to 7.2–7.4, the interaction between PTX-PBA and fructose was strengthened, which decreased the drug release *in vitro*. While this *in vitro* release profile may not fully reflect the drug release *in vivo*, it clearly demonstrated that PTX-PBA-Fru NPs exhibited sustained-release characteristics. Notably, PTX was not detected during the release process, indicating that PTX-PBA maintains excellent chemical stability.

3.5. In vitro cytotoxicity assay

The *in vitro* cytotoxicity of PTX injections, PTX-PBA injections, PBA solution, and PTX-PBA Fru NPs against 4T1 cells was evaluated using an MTT assay. As shown in Fig. 3F, the IC50 value for PTX-PBA injections was 0.90 μg/mL, which was lower than that of PTX injections at 2.14 μg/mL. This indicated that PTX-PBA exhibited stronger cytotoxicity, likely due to the interaction between the phenylboronic acid group and the sialic acid highly expressed on the surface of tumor cells [27]. This interaction may enhance the cellular uptake of PTX-PBA. Additionally, PTX-PBA Fru NPs had an IC50 value of 0.57 μg/mL, slightly lower than that of PTX-PBA injections. This effect may result from a balance between the advantages of nanoparticles in promoting cellular uptake and the potential drawback of fructose inhibiting the interaction of PTX-PBA with sialic acid on 4T1 cells. However, PBA itself exhibited minimal cytotoxic effects on mouse breast cancer cells, with an IC50 value of 398.5 μg/mL. Therefore, the cytotoxic effects of PTX-PBA are almost entirely independent of the inherent toxicity of PBA.

3.6. In vivo anti-tumor efficacy of PTX-PBA-Fru NPs

Anti-tumor evaluation: Animal experiments were conducted as outlined in Fig. 4A. The tumor volume in the NS group increased rapidly, followed by the groups receiving PTX injections and PTX-PBA injections (Fig. 4B). The tumor growth profiles for the latter two groups were similar, indicating no significant difference in anti-tumor efficacy. PTX-PBA injections did not demonstrate superior tumor inhibition compared to PTX injections. This lack of enhanced efficacy may be attributed to high levels of circulating monosaccharides occupying the binding sites of the PBA moiety or the poor tumor-targeting capability of PBA *in vivo*. Previous studies have suggested that PBA can be structurally modified (e.g., by introducing electron-withdrawing groups such as -F or -NO_2) to enhance its binding affinity with sialic acid (SA) under weakly acidic conditions [47]. Additionally, the literature indicates that

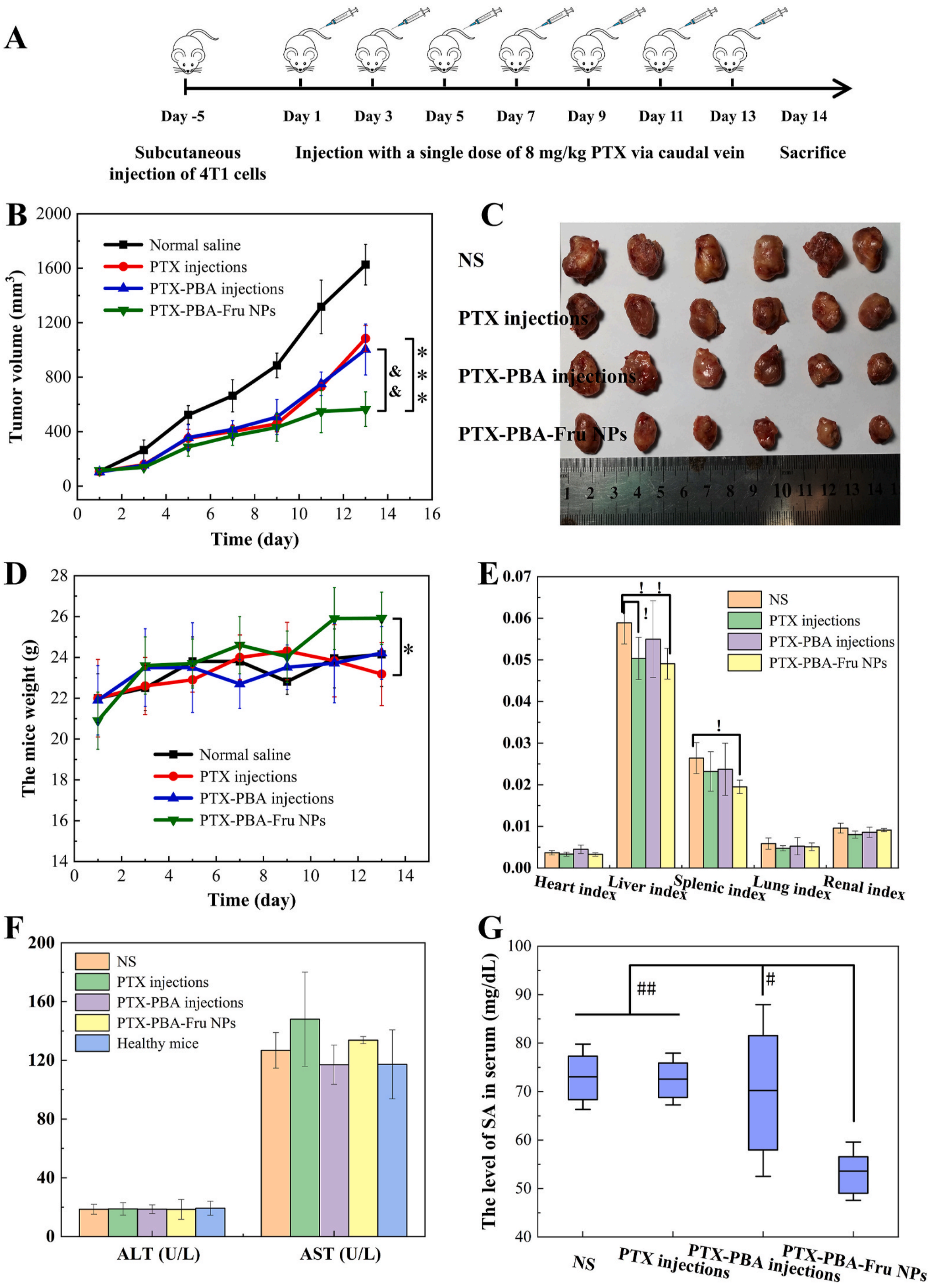

Fig. 4. *In vivo* anti-tumor efficacy of PTX-PBA-Fru NPs in 4T1 tumor-bearing mice. (A) Schematic diagram illustrating the process of the *in vivo* experiment. (B) Changes in tumor volume during administration (n = 6, error bars, SD). $^{***}p < 0.001$ compared to PTX injections; $^{\&\&}p < 0.01$ compared to PTX-PBA injections (one-way ANOVA followed by Least-Significant Difference). (C) Tumor images from different treatment groups. (D) Changes in body weight of mice during administration (n = 6, mean ± SD). $^{*}p < 0.05$ (one-way ANOVA followed by Least-Significant Difference). (E) Organ indexes for different groups. Data are presented as mean ± SD. $^{!}p < 0.05$, $^{!!}p < 0.01$, vs NS (one-way ANOVA followed by Least-Significant Difference). (F) Serum ALT and AST levels (n = 3, mean ± SD). The results were non-significant. (G) Sialic acid concentrations in serum (n = 3). Error bars, SD. $^{\#}p < 0.05$, $^{\#\#}p < 0.01$ (one-way ANOVA followed by Least—Significant Difference).

pyridine-boric acid (BPA) exhibits the strongest binding ability with SA, unaffected by co-existing sugar molecules [48]. However, attempts to synthesize PTX-BPA were unsuccessful.

In contrast, mice treated with PTX-PBA-Fru NPs exhibited significantly slower tumor growth. The tumor inhibition rate (TIR), calculated based on tumor weight (see Table 1 and Fig. 4C), demonstrated that PTX-PBA-Fru NPs provided significantly better therapeutic efficacy (60.99 %) compared to the two injection groups (34.01 % and 37.89 %, respectively). This enhanced efficacy may be attributed to the EPR effect, which facilitates greater accumulation of PTX-PBA-Fru NPs at the tumor site.

The safety of the three PTX formulations was evaluated by monitoring changes in body weight, organ indexes, and serum levels of ALT and AST. As shown in Fig. 4D, the group treated with PTX-PBA-Fru NPs exhibited a continuous and rapid increase in body weight ($p < 0.05$), indicating the best safety profile among the three formulations. In

Table 1
The tumor inhibition rate (TIR) of mice in different groups (n = 6).

Groups	TIR (%)
NS	N.A.
PTX injections	34.01
PTX-PBA injections	37.89
PTX-PBA-Fru NPs	60.99***

***p < 0.001 vs PTX-PBA injections group (one-way ANOVA followed by Least-Significant Difference).

contrast, mice treated with PTX-PBA injections, PTX injections, or NS showed similar changes in body weight. There were no significant differences in the heart, lung, and kidney indexes among all groups (Fig. 4E). However, treatments with PTX injections and PTX-PBA-Fru NPs resulted in significantly lower liver indexes compared to the NS group ($p < 0.05$ and $p < 0.01$, respectively). To further evaluate liver function, serum ALT and AST levels were measured in mice from all groups. As shown in Fig. 4F, no significant differences in ALT and AST levels were observed across the groups. The abnormal spleen index in the PTX-PBA-Fru NPs group may be attributed to the alleviation of splenomegaly caused by the tumor [49,50]. Overall, PTX-PBA-Fru NPs demonstrated good biosafety *in vivo*.

Potential ability to inhibit tumor metastasis: Serum sialic acid (SA) levels are elevated in cancer patients compared to healthy individuals [51]. Carbohydrate antigen 19-9 (CA19-9), a sialylated carbohydrate antigen, is widely used as a tumor marker in clinical diagnostics [52]. Therefore, serum SA has the potential to serve as a broad-spectrum marker for malignant tumors, reflecting their occurrence, progression, and prognosis [53].

As shown in Fig. 4G, the levels of serum SA in the NS group, the PTX injections group, and the PTX-PBA injections group were similar. In contrast, the PTX-PBA-Fru NPs group exhibited a significantly reduced serum SA concentration ($p < 0.01$ compared to PTX injections), suggesting slower tumor progression and a lower risk of metastasis in this group. This finding was supported by the dissected lungs in Fig. 5A, where no tumor metastasis was observed in the PTX-PBA-Fru NPs group, while all other groups exhibited tumor metastases. This result may be attributed to the PTX-PBA-Fru NPs inducing ICD, which activates the immune response.

ICD is a specific form of cell death that enhances the immunogenicity of dying cells and releases damage-associated molecular patterns (DAMPs), such as HMGB1 and ATP, which activate T cell-mediated antitumor immune responses [54,55]. Once released from compromised cell membranes, HMGB1 is captured by antigen-presenting cells (APCs), promoting the production of pro-inflammatory cytokines. Additionally, HMGB1 can bind to Toll-like receptors 2 or 4 (TLR2/4), stimulating innate immune cells [56]. ATP has been reported to enhance the recruitment of myeloid cells to the site of ICD by acting as a "find-me" signal for dendritic cells and macrophages [57,58]. As shown in Fig. 5B, the concentration of HMGB1 in the serum of mice treated with PTX-PBA injections was higher than that in mice treated with PTX injections or NS ($p < 0.05$). Given that PTX is known to induce ICD, it is likely that when PTX-PBA accumulates in large amounts within tumor cells by binding to sialic acid, ICD production is enhanced, leading to increased HMGB1 release. Moreover, due to the EPR effect, PTX-PBA-Fru NPs can

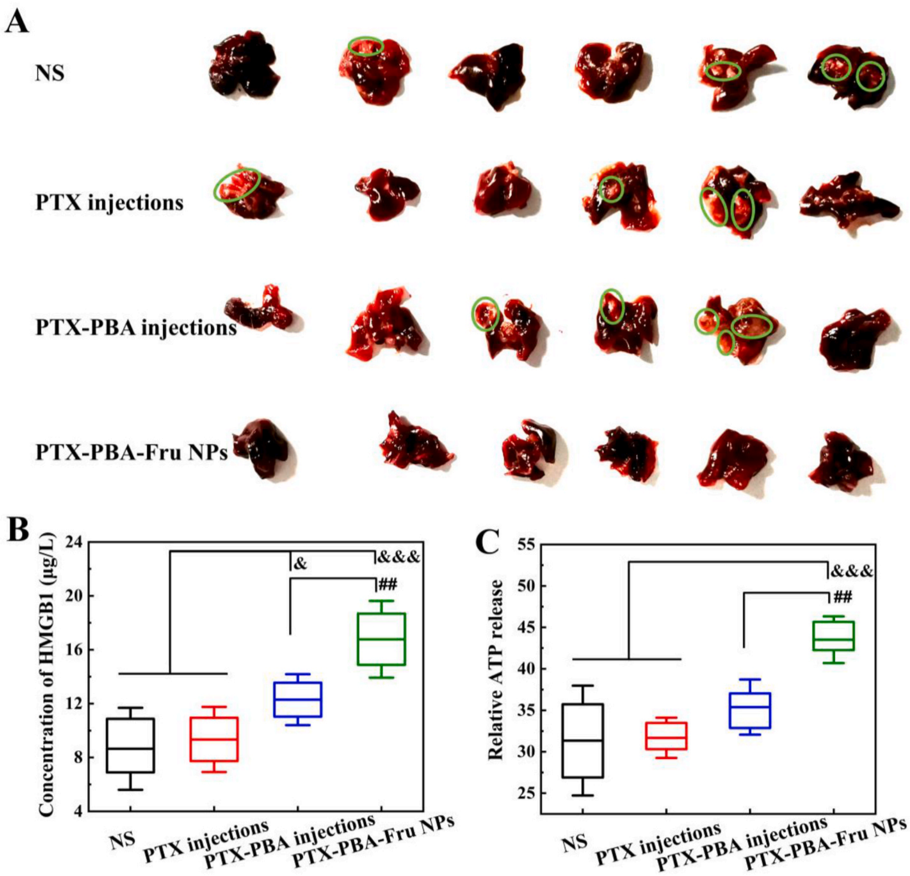

Fig. 5. The potential ability of PTX-PBA-Fru NPs to inhibit tumor metastasis by inducing immunogenic cell death (ICD). (A) Comparative analysis of pulmonary metastasis in mice among different treatment groups (n = 6). (B) Serum levels of high mobility group protein B1 (HMGB1, n = 3). (C) Adenosine triphosphate (ATP) levels in the cell culture medium (n = 3). Data are presented as mean ± SD. Statistical significance is indicated with $^{\&}p < 0.05$, $^{\&\&\&}p < 0.001$, $^{\#\#}p < 0.01$, using one-way ANOVA followed by Least-Significant Difference.

accumulate more effectively in tumors, resulting in significantly higher serum HMGB1 levels compared to the PTX injections group ($p < 0.001$) and the PTX-PBA injections group ($p < 0.01$). However, due to the instability of ATP *in vitro*, ATP levels were measured in fresh cell supernatants after drug treatment. As shown in Fig. 5C, ATP release in PTX-PBA-Fru NPs group was significantly higher than that in PTX injections and NS groups ($p < 0.001$) and in the PTX-PBA injections group ($p < 0.01$). Therefore, we conclude that PTX-PBA-Fru NPs can effectively induce ICD to enhance the anti-tumor immune response.

3.7. *In vitro BMDC activation*

Dendritic cells (DCs) are highly specialized APCs that excel in the uptake, processing, and presentation of antigens. Immature DCs possess a strong capacity for antigen phagocytosis. Upon antigen uptake, DCs undergo maturation, characterized by the upregulation of co-stimulatory molecules such as CD80 and CD86 [59]. Once mature, DCs can activate naive T cells and play a pivotal role in initiating, regulating, and sustaining the immune response.

As illustrated in Fig. 6A, the maturation of dendritic cells (DCs) decreased after PTX treatment, falling below that of the NS group, probably due to its cytotoxic effects. In contrast, the maturation of DCs following treatment with PTX-PBA-Fru NPs was significantly greater than that observed in PTX injections group ($p < 0.05$). This enhancement may be associated with the ICD effect. Dying tumor cells release DAMPs, such as HMGB1 and ATP, which bind to pattern recognition receptors on DCs, promoting their maturation [59]. R848 significantly increased the proportion of $CD80^+CD86^+$ DCs compared to the PTX-treated group ($p < 0.01$). Co-treatment with PTX-PBA-Fru NPs and R848-Lipo further enhanced the proportion of $CD86^+CD80^+$ DCs, showing a significant difference compared to the R848 solution group ($p < 0.001$). These results demonstrated that chemoimmunotherapy more effectively activated the immune response and promoted DC maturation compared to monotherapy.

3.8. *Macrophage polarization and re-education*

Tumor-associated macrophages of the M2 type create an immunosuppressive microenvironment that hinders tumor therapy. R848 can promote the polarization of M2-type macrophages into M1-type macrophages, enhancing anti-tumor immunotherapy [18,20]. As shown in Fig. 6B, the M1/M2 ratio showed no significant difference between the NS group and PTX group or PTX-PBA-Fru NPs group, indicating that chemotherapy alone has little effect on macrophage repolarization. However, R848 treatment significantly increased the M1/M2 ratio, demonstrating its ability to repolarize M2 macrophages into the M1 phenotype. Notably, the combination of PTX-PBA-Fru NPs and R848-Lipo further increased M1 macrophages, significantly elevating the M1/M2 ratio compared to the R848 solution group ($p < 0.05$). Thus, the combination of PTX-PBA-Fru NPs and R848-Lipo more effectively promoted M2-to-M1 repolarization than either immunotherapy or chemotherapy alone.

3.9. *The synergistic anti-tumor efficacy of PTX-PBA-Fru NPs and R848-Lipo*

ICD induced by PTX-PBA-Fru NPs enhances the anti-tumor immune response of R848 *in vivo*: R848, a TLR7/8 agonist, enhances chemotherapy efficacy but may cause systemic toxicity at high doses or insufficient efficacy at low doses. In preliminary experiments, combining 3.5 mg/kg R848 with 8 mg/kg PTX caused a 15 % weight loss and poor health in tumor-bearing mice, with death occurring at 5 mg/kg R848. Therefore, we administered 1.5 mg/kg R848 24 h after PTX-PBA (18.8 mg/kg) injection, as shown in Fig. 7A.

As illustrated in Fig. 7B, the NS group showed rapid tumor growth, reaching 1900 mm^3 by day 13. The PTX and PTX-PBA injection groups exhibited slower tumor growth (900 mm^3 and 800 mm^3, respectively) compared to the NS group. The PTX-PBA-Fru NPs group showed even slower growth (660 mm^3, $p < 0.05$ vs. PTX). Free R848 achieved a tumor inhibition rate of 70 %. Remarkably, the combination of R848-Lipo with PTX-PBA injections or PTX-PBA-Fru NPs nearly halted tumor growth.

After seven doses, survival was monitored. As shown in Fig. 7C and Table 2, mice treated with PTX injections had a median survival time (MST) of 19 days, longer than the NS group (15 days). PTX-PBA injections further extended MST to 24 days, and PTX-PBA-Fru NPs to 25 days. R848 alone achieved an MST of 26 days. Combination therapies achieved MSTs of 27 days (PTX-PBA + R848-Lipo) and 45 days (PTX-PBA-Fru NPs + R848-Lipo), with complete tumor eradication in 2/8 and 3/8 mice, respectively (Fig. S8). The five tumor-free mice remained healthy, reaching 28 g by day 105.

Biosafety was also assessed. As shown in Fig. 7D, the PTX-PBA-Fru NPs group showed significant weight gain ($p < 0.01$ vs. PTX). Mice treated with R848-based preparations initially lost weight due to R848 toxicity but gradually recovered, indicating adaptive tolerance.

Long-term immune memory: After the primary 4T1 tumors were eradicated, the five tumor-free mice were re-challenged with 4T1 cells on day 105, at least 75 days post-tumor eradication. As shown in Fig. 7E, the two mice in the PTX-PBA injections + R848-Lipo group exhibited rapid tumor growth after re-challenge. In contrast, the three mice in the PTX-PBA-Fru NPs + R848-Lipo group developed small tumors (<20 mm^3) by day 4, which completely disappeared by day 7. No tumor recurrence was observed, and the mice remained healthy throughout the 21-day observation period. These results demonstrate that the PTX-PBA-Fru NPs + R848-Lipo treatment holds significant potential for clinical tumor therapy.

3.10. *In vivo immune activation*

To evaluate whether treatment with PTX-PBA-Fru NPs or their combination with R848-Lipo improves the immunosuppressive tumor microenvironment, we analyzed the levels of $CD3^+$, $CD4^+$ and $CD8^+$ T cells, as well as the M1/M2 macrophage ratio in tumor tissues using flow cytometry. The gating strategies were shown in Fig. S9. As illustrated in Fig. 8A–B and Fig. S10, the levels of $CD3^+$, $CD4^+$, and $CD8^+$ T cell infiltration, as well as the M1/M2 macrophage ratio in tumor tissues after PTX-PBA-Fru NPs treatment, were similar to those in the NS and PTX groups, likely due to insufficient ICD effects to alter the tumor microenvironment *in vivo*. After R848 solution treatment, $CD3^+$ and $CD4^+$ T cells increased ($p < 0.05$), but no significant difference was observed compared to the PTX-PBA-Fru NPs and R848-Lipo group. However, the combination of PTX-PBA-Fru NPs and R848-Lipo significantly increased $CD8^+$ T cells and the M1/M2 macrophage ratio compared to R848 alone ($p < 0.05$). This indicated that 1.5 mg/kg of R848 promoted $CD3^+$ and $CD4^+$ T cell infiltration but was less effective than the chemo-immunotherapy combination in enhancing $CD8^+$ T cells and repolarizing macrophages.

Immunofluorescence staining of tumor tissue (Fig. 8C) provides further insights. Compared to PTX injections, the PTX-PBA-Fru NPs group showed a notable increase in M1-type macrophages (iNOS, red). In the PTX-PBA-Fru NPs + R848-Lipo group, M1 macrophages were further elevated, while M2 macrophages (CD206, green) decreased significantly. Numerous apoptotic bodies and fragmented nuclei were observed, indicating widespread apoptosis within the tumor tissue. Additionally, PTX-PBA-Fru NPs and free R848 promoted the upregulation of pro-inflammatory cytokines IL-12 and TNF-α (Fig. 8D). However, the combination therapy of PTX-PBA-Fru NPs and R848-Lipo resulted in a robust release of IL-12 and TNF-α, further enhancing the anti-tumor effect.

To assess whether the combination of PTX-PBA-Fru NPs and R848-Lipo induced long-term immune memory, we analyzed memory T cells in the spleen using flow cytometry. The gating strategy was shown in Fig. S11. As shown in Fig. 8E–F, the number of memory T cells in the

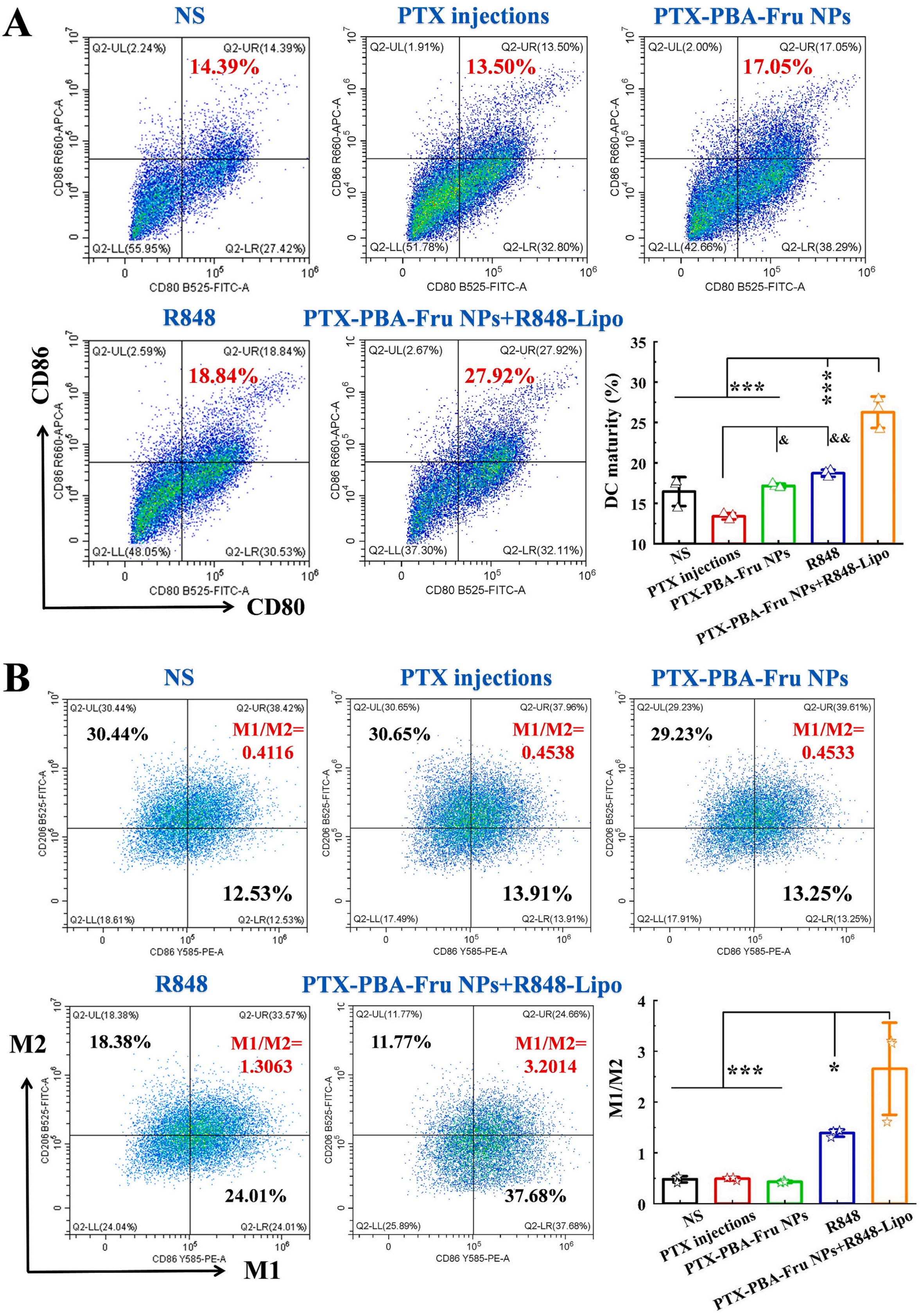

Fig. 6. Immunological analysis *in vitro* (n = 3). (A) Flow cytometry analysis and quantification of CD80 and CD86 double-positive DC cells. (B) Flow cytometry analysis of M1 macrophages ($CD86^+$ $CD206^-$) and M2 macrophages ($CD86^-$ $CD206^+$) in BMDM cells following various treatments and the corresponding ratio of M1/M2. Data are presented as mean ± SD. Statistical significance is indicated as $^{\&}p < 0.05$, $^{\&\&}p < 0.01$ vs PTX injections; $^{*}p < 0.05$, $^{***}p < 0.001$ vs PTX-PBA-Fru NPs + R848-Lipo (one-way ANOVA followed by Tukey's multiple comparisons test).

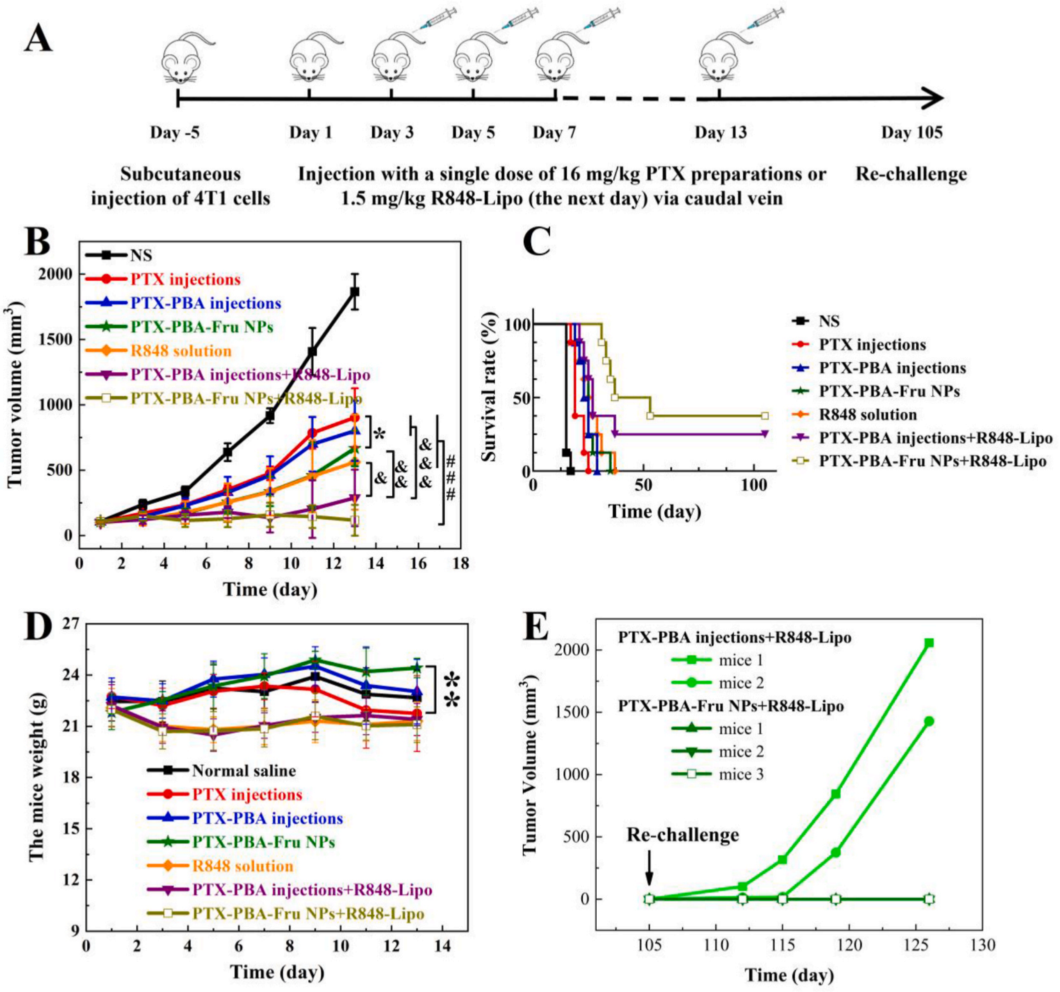

Fig. 7. Anti-tumor efficacy of PTX-PBA-Fru NPs combined with R848-Lipo in 4T1 tumor-bearing mice (n = 8). (A) Schematic diagram of the experimental procedure. (B) Changes in tumor volume over time during administration. Error bars, SD. $^{*}p < 0.05$, vs PTX-PBA-Fru NPs; $^{\&}p < 0.05$, $^{\&\&}p < 0.01$, $^{\&\&\&}p < 0.001$, vs PTX-PBA injections + R848-Lipo; $^{\#\#\#}p < 0.001$, vs PTX-PBA-Fru NPs + R848-Lipo (one-way ANOVA followed by Least-Significant Difference). (C) The survival rate of mice in each group. (D) Changes in body weight of mice during administration. Error bars, SD. $^{**}p < 0.01$ (one-way ANOVA followed by Least-Significant Difference). (E) Mice cured of primary 4T1 tumors were re-challenged with a subcutaneous injection of 2×10^6 4T1 cells. Tumor volume was measured for three weeks.

Table 2
The median survival time of each group after treatment (n = 8).

	NS	PTX injections	PTX-PBA injections	PTX-PBA-Fru NPs	R848 solution	PTX-PBA injections + R848-Lipo	PTX-PBA-Fru NPs + R848-Lipo
Survival rate	0/8	0/8	0/8	0/8	0/8	2/8	3/8
Median survival time (days)	15	19	24	25	26	27	45

spleen of mice treated with R848 (1.5 mg/kg) was not significantly different from that in the chemotherapy or NS group, suggesting that the ability of R848 to promote immune memory was insufficient at low dose. However, PTX-PBA-Fru NPs and R848-Lipo treatment increased memory T cells obviously, demonstrating its ability to effectively induce anti-tumor immune memory.

3.11. Safety evaluation

Anaphylaxis evaluation of PTX-PBA-Fru NPs: Cremophor EL in paclitaxel injections is known to cause severe allergic reactions in clinical settings, including dyspnea, flushing, rash, tachycardia, hypotension, and systemic urticaria [60]. IgE-mediated anaphylaxis is a life-threatening immune response triggered by allergens, including drugs. Upon allergen activation, IgE-bound mast cells undergo degranulation, releasing and synthesizing active mediators that promote vasodilation and vascular permeability, leading to a rapid decrease in blood pressure and body temperature [40,61]. In this study, mice receiving PTX injections at an equivalent dose of 16 mg/kg exhibited allergic symptoms such as restlessness, erect hair, and unstable gait. In contrast, mice in the NS and PTX-PBA-Fru NPs groups showed no allergic symptoms. As shown in Table S4, the anal temperature of mice in the PTX injections group dropped significantly from 36.1 °C to 34.4 °C within 3 h post-administration, while the normal temperature is approximately 36.2 °C. The temperature of mice in the PTX-PBA-Fru NPs group remained stable at around 36.0 °C.

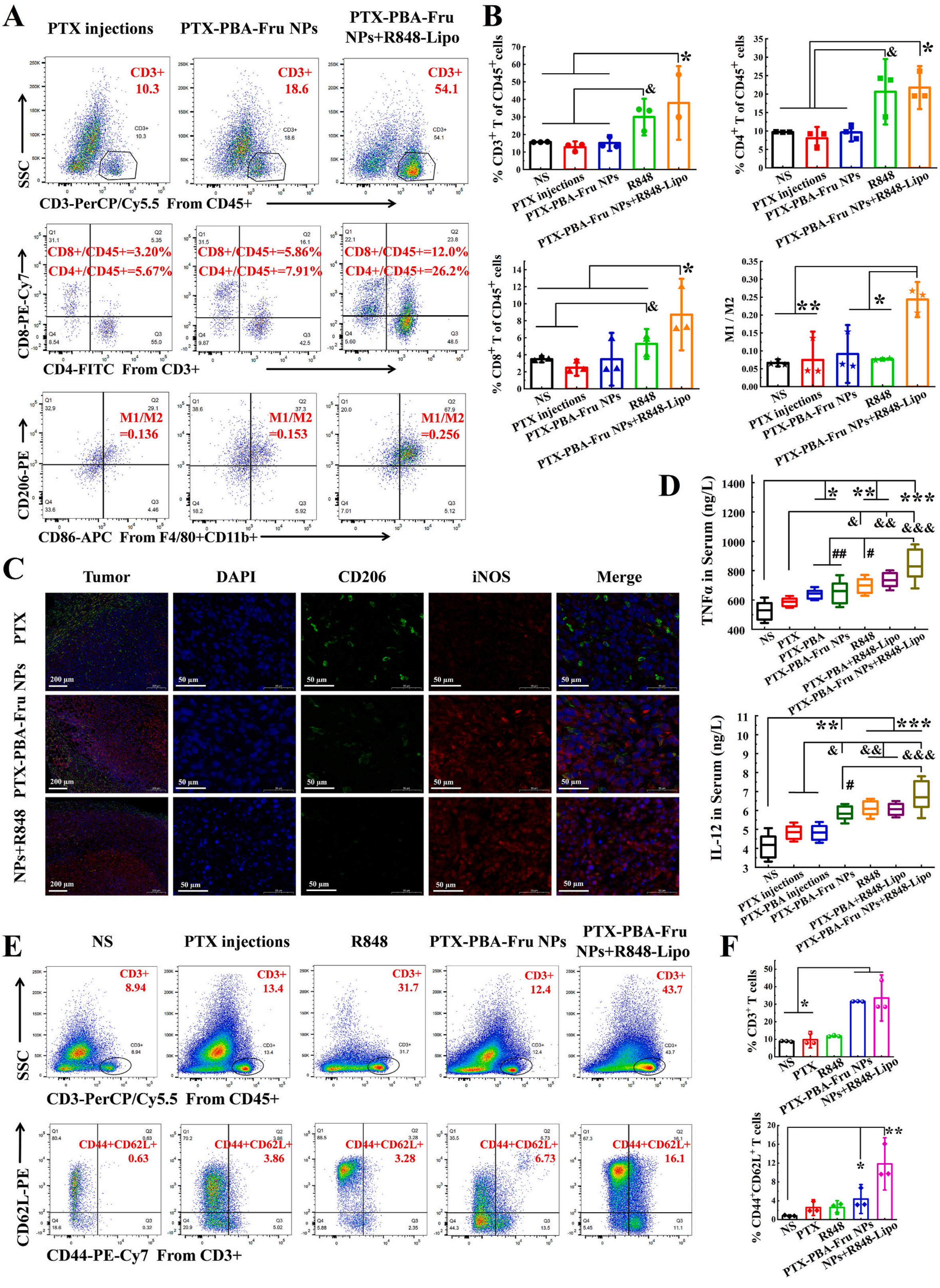

Fig. 8. Analysis of immune activation *in vivo*. (A) Flow cytometry plots and (B) levels of $CD3^+$, $CD4^+$, and $CD8^+$ T cell infiltration, as well as the M1 to M2 macrophage ratio in tumor tissues (n = 3). $^*p < 0.05$, $^{**}p < 0.01$, $^{\&}p < 0.05$ (Median test or the independent samples *t*-test) (C) Immunofluorescence staining of iNOS (M1, red) and CD206 (M2, green) in tumor tissues (scale bar, 200 μm and 50 μm, respectively). (D) Serum levels of IL-12 and TNF-α after various treatments (n = 3). $^*p < 0.05$, $^{**}p < 0.01$, $^{***}p < 0.001$; $^{\&}p < 0.05$, $^{\&\&}p < 0.01$, $^{\&\&\&}p < 0.001$; $^{\#}p < 0.05$, $^{\#\#}p < 0.05$ (one-way ANOVA followed by Least-Significant Difference) (E) Flow cytometry plots and (F) levels of $CD3^+$ and memory T cells ($CD44^+CD62L^+$) in the spleen (n = 3). Error bars represent SD. Statistical significance: $^*p < 0.05$, $^{**}p < 0.01$ (Kruskal-Wallis test). (For interpretation of the references to color in this figure legend, the reader is referred to the Web version of this article.)

In addition to body temperature, vascular permeability is considered the gold standard for diagnosing anaphylaxis. As illustrated in Fig. S12, no whole-body blue extravasation was observed in the NS group or the PTX-PBA-Fru NPs group. In contrast, the PTX injections group exhibited noticeable blue oozing in the ears, mouth, eyelids, and feet. These results demonstrate that PTX-PBA-Fru NPs did not induce allergic reactions in this experiment.

Maximum tolerated dose (MTD): The MTDs of Taxol and Abraxane in female nude mice, as reported in the literature, are 20 mg/kg and 90 mg/kg, respectively [62]. In this study, the MTD of PTX injections was determined to be 40 mg/kg (Table S5), higher than previously reported, likely due to the greater drug tolerance of Balb/c mice compared to nude mice. In contrast, PTX-PBA-Fru NPs demonstrated significantly lower toxicity, with an MTD of 200 mg/kg, five times higher than that of PTX injections. Mice in the PTX injections group at 50 mg/kg and the PTX-PBA-Fru NPs group at 400 mg/kg experienced significant weight loss and mortality. These findings suggest that PTX-PBA-Fru NPs exhibit enhanced safety compared to conventional paclitaxel injections, offering potential for improving the clinical therapeutic dosing of PTX.

4. Conclusion

In this study, a PTX derivative, PTX-PBA, was synthesized. It exhibited anti-tumor activity similar to PTX and readily co-assembled with fructose into PTX-PBA-Fru NPs, which could be directly administered intravenously and demonstrated significantly better anti-tumor efficacy than free PTX and free PTX-PBA. Beyond direct tumor growth inhibition, PTX-PBA-Fru NPs also induced a robust ICD effect. When combined with R848 liposomes, they synergistically achieved strong anti-tumor immune activation and long-term immune memory, resulting in a tumor eradication rate of 37.5 % and subsequent immunity against tumor re-challenge.

Unlike previously reported PTX nanomedicines, PTX-PBA-Fru NPs were entirely assembled from small molecules without the use of macromolecular excipient. Such nanomedicines offer several notable advantages: (1) high drug loading capacity (up to 84.7 %), (2) ease of preparation and suitability for industrial production, (3) low production costs, (4) excellent biosafety *in vivo*, with no allergic reactions or potential immunogenicity associated with macromolecular excipients. Marketed PTX formulations typically contain either allergic solvents or large quantities of polymeric excipients. In contrast, PTX-PBA-Fru NPs represent a novel intravenous PTX formulation free of solvents or polymeric excipients, with promising potential for clinic application.

Our studies have demonstrated that PTX-PBA exhibits a strong synergistic anti-tumor effect when combined with R848. However, the optimal ratio between these two agents for maximal therapeutic efficacy remains to be determined. Future studies will systematically explore different drug ratios and the most effective delivery systems for them to further enhance tumor treatment outcomes. We have developed an advanced therapeutic strategy by co-formulating PTX-PBA-Fru NPs and liposomal R848 into an injectable hydrogel, which has been applied to post-surgical wounds to prevent tumor recurrence and metastasis. The details and the results of this research will be published separately. In addition, chemotherapeutics-PBA conjugates and chemotherapeutics-PBA-Fru NPs may provide a promising and universal strategy for preparing nanomedicines from current chemotherapeutics. Related work is ongoing.

CRediT authorship contribution statement

Manzhen Li: Writing – original draft, Methodology, Formal analysis, Data curation, Conceptualization. **Likang Lu:** Methodology, Investigation, Data curation. **Yaoyao Guo:** Software, Investigation, Formal analysis. **Jingxin Fu:** Visualization, Methodology. **Ziqi Zhang:** Software, Data curation. **Pengxin Li:** Visualization, Validation. **Yifei Guo:** Supervision, Resources. **Meihua Han:** Supervision, Resources. **Xiangtao Wang:** Writing – review & editing, Project administration, Funding acquisition, Conceptualization.

Availability of data and materials

The datasets generated and/or analyzed during the current study are available from the corresponding author upon reasonable request.

Funding

This work was supported by the CAMS Innovation Fund for Medical Sciences (CIFMS) (No. 2021-I2M-1–071).

Declaration of competing interest

The authors declare that they have no known competing financial interests or personal relationships that could have appeared to influence the work reported in this paper.

Abbreviations

PTX	paclitaxel
PTX-PBA	phenylboronic acid-modified paclitaxel derivative
R848	resiquimod
Fru	fructose
PBS	phosphate buffered saline
FBS	Fetal bovine serum
ICD	immunogenic cell death
MTD	maximum tolerated dose
MST	median survival time
BMDCs	bone marrow-derived dendritic cells
BMDMs	bone marrow-derived macrophages

Appendix A. Supplementary data

Supplementary data to this article can be found online at https://doi.org/10.1016/j.mtbio.2025.101793.

Data availability

Data will be made available on request.

References

[1] F.Y. Alqahtani, F.S. Aleanizy, E. El Tahir, H.M. Alkahtani, B.T. AlQuadeib, Paclitaxel, profiles drug subst excip, Relat Methodol 44 (2019) 205–238, https://doi.org/10.1016/bs.podrm.2018.11.001.

[2] S. Zhang, T. Ye, Y. Liu, G. Hou, Q. Wang, F. Zhao, et al., Research advances in clinical applications, anticancer mechanism, total chemical synthesis, semi-synthesis and biosynthesis of paclitaxel, Molecules 28 (2023), https://doi.org/10.3390/molecules28227517.

[3] C. Nehate, S. Jain, A. Saneja, V. Khare, N. Alam, R.D. Dubey, et al., Paclitaxel formulations: challenges and novel delivery options, Curr. Drug Deliv. 11 (2014) 666–686, https://doi.org/10.2174/1567201811666140609154949.

[4] A.M. Sofias, M. Dunne, G. Storm, C. Allen, The battle of "nano" paclitaxel, Adv. Drug Deliv. Rev. 122 (2017) 20–30, https://doi.org/10.1016/j.addr.2017.02.003.

[5] S. Koudelka, J. Turánek, Liposomal paclitaxel formulations, J Control Release 163 (2012) 322–334, https://doi.org/10.1016/j.jconrel.2012.09.006.

[6] M. Yang, Z. Zhang, P. Jin, K. Jiang, Y. Xu, F. Pan, et al., Effects of PEG antibodies on in vivo performance of LNP-mRNA vaccines, Int J Pharm 650 (2024) 123695, https://doi.org/10.1016/j.ijpharm.2023.123695.

[7] X. Huang, P. Wang, T. Li, X. Tian, W. Guo, B. Xu, et al., Self-assemblies based on traditional medicine berberine and cinnamic acid for adhesion-induced inhibition multidrug-resistant Staphylococcus aureus, ACS Appl. Mater. Interfaces 12 (2020) 227–237, https://doi.org/10.1021/acsami.9b17722.

[8] S. Fu, X. Yi, Y. Li, Y. Li, X. Qu, P. Miao, et al., Berberine and chlorogenic acid-assembled nanoparticles for highly efficient inhibition of multidrug-resistant Staphylococcus aureus, J. Hazard Mater. 473 (2024) 134680, https://doi.org/10.1016/j.jhazmat.2024.134680.

[9] X. Guo, W. Luo, L. Wu, L. Zhang, Y. Chen, T. Li, et al., Natural products from herbal medicine self-assemble into advanced bioactive materials, Adv. Sci. (Weinh.) 11 (2024) e2403388, https://doi.org/10.1002/advs.202403388.

[10] L. Han, T. Wang, J. Wu, X. Yin, H. Fang, N. Zhang, A facile route to form self-carried redox-responsive vorinostat nanodrug for effective solid tumor therapy, Int J Nanomedicine 11 (2016) 6003–6022, https://doi.org/10.2147/ijn.S118727.

[11] X. Han, J. Chen, M. Jiang, N. Zhang, K. Na, C. Luo, et al., Paclitaxel-paclitaxel prodrug nanoassembly as a versatile nanoplatform for combinational cancer therapy, ACS Appl. Mater. Interfaces 8 (2016) 33506–33513, https://doi.org/10.1021/acsami.6b13057.

[12] J. Liu, X. Li, Y. Li, Q. Gong, K. Luo, Metformin-based nanomedicines for reprogramming tumor immune microenvironment, Theranostics 15 (2025) 993–1016, https://doi.org/10.7150/thno.104872.

[13] J. Liu, Y. Bai, Y. Li, X. Li, K. Luo, Reprogramming the immunosuppressive tumor microenvironment through nanomedicine: an immunometabolism perspective, EBioMedicine 107 (2024) 105301, https://doi.org/10.1016/j.ebiom.2024.105301.

[14] Z. Li, X. Lai, S. Fu, L. Ren, H. Cai, H. Zhang, et al., Immunogenic cell death activates the tumor immune microenvironment to boost the immunotherapy efficiency, Adv. Sci. (Weinh.) 9 (2022) e2201734, https://doi.org/10.1002/advs.202201734.

[15] Y. Li, Y. Wu, Z. Fang, Y. Zhang, H. Ding, L. Ren, et al., Dendritic nanomedicine with boronate bonds for augmented chemo-immunotherapy via synergistic modulation of tumor immune microenvironment, Adv Mater 36 (2024) e2307263, https://doi.org/10.1002/adma.202307263.

[16] J. Sun, Z. Liu, H. Yao, H. Zhang, M. Zheng, N. Shen, et al., Azide-masked resiquimod activated by hypoxia for selective tumor therapy, Adv Mater 35 (2023) e2207733, https://doi.org/10.1002/adma.202207733.

[17] H. Li, M. Somiya, S. Kuroda, Enhancing antibody-dependent cellular phagocytosis by Re-education of tumor-associated macrophages with resiquimod-encapsulated liposomes, Biomaterials 268 (2021) 120601, https://doi.org/10.1016/j.biomaterials.2020.120601.

[18] C.B. Rodell, S.P. Arlauckas, M.F. Cuccarese, C.S. Garris, R. Li, M.S. Ahmed, et al., TLR7/8-agonist-loaded nanoparticles promote the polarization of tumour-associated macrophages to enhance cancer immunotherapy, Nat. Biomed. Eng. 2 (2018) 578–588, https://doi.org/10.1038/s41551-018-0236-8.

[19] B. Bahmani, H. Gong, B.T. Luk, K.J. Haushalter, E. DeTeresa, M. Previti, et al., Intratumoral immunotherapy using platelet-cloaked nanoparticles enhances antitumor immunity in solid tumors, Nat. Commun. 12 (2021) 1999, https://doi.org/10.1038/s41467-021-22311-z.

[20] C.B. Rodell, M.S. Ahmed, C.S. Garris, M.J. Pittet, R. Weissleder, Development of adamantane-conjugated TLR7/8 agonists for supramolecular delivery and cancer immunotherapy, Theranostics 9 (2019) 8426–8436, https://doi.org/10.7150/thno.35434.

[21] R. Lu, C. Groer, P.A. Kleindl, K.R. Moulder, A. Huang, J.R. Hunt, et al., Formulation and preclinical evaluation of a toll-like receptor 7/8 agonist as an anti-tumoral immunomodulator, J Control Release 306 (2019) 165–176, https://doi.org/10.1016/j.jconrel.2019.06.003.

[22] Q. Zhao, L. Lu, Q. Shen, Direct monofluoromethylthiolation with S-(Fluoromethyl) benzenesulfonothioate, Angew Chem. Int. Ed. Engl. 56 (2017) 11575–11578, https://doi.org/10.1002/anie.201705633.

[23] A.B. Lutjen, M.A. Quirk, E.M. Kolonko, Synthesis of esters via a greener steglich esterification in acetonitrile, J. Vis. Exp. (2018), https://doi.org/10.3791/58803.

[24] S.J. Coutts, J. Adams, D. Krolikowski, R.J. Snow, Two efficient methods for the cleavage of pinanediol boronate esters yielding the free boronic acids, Tetrahedron Lett. 35 (1994) 5109–5112.

[25] D. Jia, Y. Lu, M. Lv, F. Wang, X. Lu, W. Zhu, et al., Targeted co-delivery of resiquimod and a SIRPα variant by liposomes to activate macrophage immune responses for tumor immunotherapy, J Control Release 360 (2023) 858–871, https://doi.org/10.1016/j.jconrel.2023.07.030.

[26] G. Pauli, P.H. Chao, Z. Qin, R. Böttger, S.E. Lee, S.D. Li, Liposomal resiquimod for enhanced immunotherapy of peritoneal metastases of colorectal cancer, Pharmaceutics 13 (2021), https://doi.org/10.3390/pharmaceutics13101696.

[27] M. Li, M. Chen, P. Li, Z. Zhang, H. Yu, X. Wang, Enhanced transcytosis and therapeutic efficacy of paclitaxel nanoparticles: pyridylboronic acid modification and sialic acid targeting, Colloids Surf. B Biointerfaces 247 (2025) 114417, https://doi.org/10.1016/j.colsurfb.2024.114417.

[28] J.G. Brandenburg, C. Bannwarth, A. Hansen, S. Grimme, B97-3c: a revised low-cost variant of the B97-D density functional method, J. Chem. Phys. 148 (2018) 064104, https://doi.org/10.1063/1.5012601.

[29] C. Bannwarth, E. Caldeweyher, S. Ehlert, A. Hansen, P. Pracht, J. Seibert, et al., Extended tight-binding quantum chemistry methods, Wiley Interdiscip. Rev. Comput. Mol. Sci. 11 (2021) e1493.

[30] F. Neese, Software update: the ORCA program system, version 4.0, Wiley Interdiscip. Rev. Comput. Mol. Sci. 8 (2018) e1327.

[31] F. Neese, The ORCA program system, Wiley Interdiscip. Rev. Comput. Mol. Sci. 2 (2012) 73–78.

[32] H. Kruse, S. Grimme, A geometrical correction for the inter-and intra-molecular basis set superposition error in Hartree-Fock and density functional theory calculations for large systems, The Journal of chemical physics 136 (2012).

[33] J.G. Brandenburg, M. Alessio, B. Civalleri, M.F. Peintinger, T. Bredow, S. Grimme, Geometrical correction for the inter-and intramolecular basis set superposition error in periodic density functional theory calculations, J. Phys. Chem. 117 (2013) 9282–9292.

[34] S. Grimme, J.G. Brandenburg, C. Bannwarth, A. Hansen, Consistent structures and interactions by density functional theory with small atomic orbital basis sets, The Journal of chemical physics 143 (2015).

[35] C. Lefebvre, H. Khartabil, J.C. Boisson, J. Contreras-García, J.P. Piquemal, E. Hénon, The independent gradient model: a new approach for probing strong and weak interactions in molecules from wave function calculations, ChemPhysChem 19 (2018) 724–735.

[36] T. Lu, F. Chen, Multiwfn: a multifunctional wavefunction analyzer, J. Comput. Chem. 33 (2012) 580–592.

[37] W. Humphrey, A. Dalke, K. Schulten, VMD: visual molecular dynamics, J. Mol. Graph. 14 (33–38) (1996) 27–38, https://doi.org/10.1016/0263-7855(96)00018-5.

[38] X. Wang, X. Liu, Y. Guo, T. Gong, W. Lu, M. Han, et al., The remarkable anti-breast cancer efficacy and anti-metastasis by multifunctional nanoparticles Co-loading squamocin, R848 and IR 780, Int J Nanomedicine 19 (2024) 4679–4699, https://doi.org/10.2147/ijn.S448860.

[39] M. Wang, D. Hu, Y. Yang, K. Shi, J. Li, Q. Liu, et al., Enhanced chemo-immunotherapy strategy utilizing injectable thermosensitive hydrogel for the treatment of diffuse peritoneal metastasis in advanced colorectal cancer, Adv. Sci. (Weinh.) 10 (2023) e2303819, https://doi.org/10.1002/advs.202303819.

[40] K. Liu, S. Lin, X. Gao, S. Wang, Y. Liu, Q. Liu, et al., Reduced allergenicity of shrimp (Penaeus vannamei) by altering the protein fold, digestion susceptibility, and allergen epitopes, J. Agric. Food Chem. 71 (2023) 9120–9134, https://doi.org/10.1021/acs.jafc.3c01557.

[41] D. Hao, Q. Meng, B. Jiang, S. Lu, X. Xiang, Q. Pei, et al., Hypoxia-activated PEGylated paclitaxel prodrug nanoparticles for potentiated chemotherapy, ACS Nano 16 (2022) 14693–14702, https://doi.org/10.1021/acsnano.2c05341.

[42] Z. Meng, Q. Lv, J. Lu, H. Yao, X. Lv, F. Jiang, et al., Prodrug strategies for paclitaxel, Int. J. Mol. Sci. 17 (2016), https://doi.org/10.3390/ijms17050796.

[43] Y. Ueda, A.B. Mikkilineni, J.O. Knipe, W.C. Rose, A.M. Casazza, D.M. Vyas, Novel water soluble phosphate prodrugs of Taxol® possessing in vivo antitumor activity, Bioorg. Med. Chem. Lett 3 (1993) 1761–1766.

[44] P. Shan, T. Ye, Y.D. Tang, H. Song, C. Wang, K. Zhu, et al., First total synthesis, antitumor evaluation and target identification of mornaphthoate E: a new tubulin inhibitor template acting on PI3K/Akt signaling pathway, Acta Pharm. Sin. B 14 (2024) 2177–2193, https://doi.org/10.1016/j.apsb.2024.02.012.

[45] T. Ghosh, A.K. Das, Dynamic boronate esters cross-linked guanosine hydrogels: a promising biomaterial for emergent applications, Coord. Chem. Rev. 488 (2023) 215170, https://doi.org/10.1016/j.ccr.2023.215170.

[46] B.K. Shull, D.E. Spielvogel, G. Head, R. Gopalaswamy, S. Sankar, K. Devito, Studies on the structure of the complex of the boron neutron capture therapy drug, L-p-boronophenylalanine, with fructose and related carbohydrates: chemical and 13C NMR evidence for the beta-D-fructofuranose 2,3,6-(p-phenylalanylorthoboronate) structure, J Pharm Sci 89 (2000) 215–222, https://doi.org/10.1002/(sici)1520-6017(200002)89:2<215::Aid-jps8>3.0.Co;2-p.

[47] J. Yan, G. Springsteen, S. Deeter, B. Wang, The relationship among pKa, pH, and binding constants in the interactions between boronic acids and diols—it is not as simple as it appears, Tetrahedron 60 (2004) 11205–11209.

[48] A. Matsumoto, A.J. Stephenson-Brown, T. Khan, T. Miyazawa, H. Cabral, K. Kataoka, et al., Heterocyclic boronic acids display sialic acid selective binding in a hypoxic tumor relevant acidic environment, Chem. Sci. 8 (2017) 6165–6170, https://doi.org/10.1039/c7sc01905j.

[49] V. Revuri, S.K. Rajendrakumar, M.S. Park, A. Mohapatra, S. Uthaman, J. Mondal, et al., Heat-confined tumor-docking reversible thermogel potentiates systemic antitumor immune response during near-infrared photothermal ablation in triple-negative breast cancer, Adv Healthc Mater 10 (2021) e2100907, https://doi.org/10.1002/adhm.202100907.

[50] X.Y. Chen, M.Y. Yan, Q. Liu, B.X. Yu, Y. Cen, S.Y. Li, Chimeric peptide engineered bioregulator for metastatic tumor immunotherapy through macrophage polarization and phagocytosis restoration, ACS Nano 17 (2023) 16056–16068, https://doi.org/10.1021/acsnano.3c04778.

[51] Z. Zhang, M. Wuhrer, S. Holst, Serum sialylation changes in cancer, Glycoconj. J. 35 (2018) 139–160, https://doi.org/10.1007/s10719-018-9820-0.

[52] S. Scarà, P. Bottoni, R. Scatena, CA 19-9: biochemical and clinical aspects, Adv. Exp. Med. Biol. 867 (2015) 247–260, https://doi.org/10.1007/978-94-017-7215-0_15.

[53] L.K. Shewell, C.J. Day, J.R. Kutasovic, J.L. Abrahams, J. Wang, J. Poole, et al., N-glycolylneuraminic acid serum biomarker levels are elevated in breast cancer patients at all stages of disease, BMC Cancer 22 (2022) 334, https://doi.org/10.1186/s12885-022-09428-0.

[54] J. Kim, M.P. Manspeaker, S.N. Thomas, Augmenting the synergies of chemotherapy and immunotherapy through drug delivery, Acta Biomater. 88 (2019) 1–14, https://doi.org/10.1016/j.actbio.2019.02.012.

[55] M. Jiang, J. Zeng, L. Zhao, M. Zhang, J. Ma, X. Guan, et al., Chemotherapeutic drug-induced immunogenic cell death for nanomedicine-based cancer chemo-immunotherapy, Nanoscale 13 (2021) 17218–17235, https://doi.org/10.1039/d1nr05512g.

[56] S. Rameshbabu, B.W. Labadie, A. Argulian, A. Patnaik, Targeting innate immunity in cancer therapy, Vaccines (Basel) 9 (2021), https://doi.org/10.3390/vaccines9020138.

[57] Z. Huang, Y. Wang, D. Yao, J. Wu, Y. Hu, A. Yuan, Nanoscale coordination polymers induce immunogenic cell death by amplifying radiation therapy mediated oxidative stress, Nat. Commun. 12 (2021) 145, https://doi.org/10.1038/s41467-020-20243-8.

[58] A.I. Birmpilis, A. Paschalis, A. Mourkakis, P. Christodoulou, I.V. Kostopoulos, E. Antimissari, et al., Immunogenic cell death, DAMPs and prothymosin α as a putative anticancer immune response biomarker, Cells (2022) 11, https://doi.org/10.3390/cells11091415.

[59] A. Del Prete, V. Salvi, A. Soriani, M. Laffranchi, F. Sozio, D. Bosisio, et al., Dendritic cell subsets in cancer immunity and tumor antigen sensing, Cell. Mol. Immunol. 20 (2023) 432–447, https://doi.org/10.1038/s41423-023-00990-6.

[60] H. Gelderblom, J. Verweij, K. Nooter, A. Sparreboom, Cremophor EL: the drawbacks and advantages of vehicle selection for drug formulation, Eur. J. Cancer 37 (2001) 1590–1598, https://doi.org/10.1016/s0959-8049(01)00171-x.

[61] C. Bao, O. Chen, H. Sheng, J. Zhang, Y. Luo, B.W. Hayes, et al., A mast cell-thermoregulatory neuron circuit axis regulates hypothermia in anaphylaxis, Sci Immunol 8 (2023) eadc9417, https://doi.org/10.1126/sciimmunol.adc9417.

[62] Z. He, X. Wan, A. Schulz, H. Bludau, M.A. Dobrovolskaia, S.T. Stern, et al., A high capacity polymeric micelle of paclitaxel: implication of high dose drug therapy to safety and in vivo anti-cancer activity, Biomaterials 101 (2016) 296–309, https://doi.org/10.1016/j.biomaterials.2016.06.002.